Monthly Notices of the ROYAL ASTRONOMICAL SOCIETY

MNRAS **463,** 3783–3798 (2016)
Advance Access publication 2016 September 7

doi:10.1093/mnras/stw2243

Improving the modelling of redshift-space distortions – II. A pairwise velocity model covering large and small scales

Davide Bianchi,[1,2★] Will J. Percival[1] and Julien Bel[2,3]

[1] *Institute of Cosmology and Gravitation, Dennis Sciama Building, University of Portsmouth, Portsmouth PO1 3FX, UK*
[2] *INAF – Osservatorio Astronomico di Brera, via Emilio Bianchi 46, I-23807 Merate, Italy*
[3] *Aix Marseille Univ, Univ Toulon, CNRS, CPT, 13009 Marseille, France*

Accepted 2016 September 4. Received 2016 July 25; in original form 2016 February 11

ABSTRACT

We develop a model for the redshift-space correlation function, valid for both dark matter particles and haloes on scales $>5\,h^{-1}$ Mpc. In its simplest formulation, the model requires the knowledge of the first three moments of the line-of-sight pairwise velocity distribution plus two well-defined dimensionless parameters. The model is obtained by extending the Gaussian–Gaussianity prescription for the velocity distribution, developed in a previous paper, to a more general concept allowing for local skewness, which is required to match simulations. We compare the model with the well-known Gaussian streaming model and the more recent Edgeworth streaming model. Using *N*-body simulations as a reference, we show that our model gives a precise description of the redshift-space clustering over a wider range of scales. We do not discuss the theoretical prescription for the evaluation of the velocity moments, leaving this topic to further investigation.

Key words: cosmology: theory – dark energy – large-scale structure of Universe.

1 INTRODUCTION

The large-scale structure of the universe is the result of a continuous infall process in which the peculiar velocity flows induced by gravitational instability drive matter towards denser regions, thus amplifying primordial density fluctuations. Peculiar velocities leave a characteristic imprint, known as 'redshift space distortions' (RSD; Kaiser 1987), on the galaxy clustering pattern measured by redshift surveys (see Hamilton 1998, for a review). If properly modelled, measurements of RSD provide a powerful way to constrain fundamental cosmological parameters in the ΛCDM paradigm or to search for evidences of deviations from this standard scenario.

The effects of RSD on the observed galaxy correlation function can be summarized as follows. On large scales, the dominant contribution is given by the coherent movement of galaxies towards overdense regions, such as clusters, walls and filaments, and away from voids. This 'squashes' the iso-correlation contours along the line of sight. As we move to smaller scales, the disordered motion of galaxies inside those formed structures becomes increasingly important, resulting in elongated iso-contours along the line of sight, usually referred to as 'fingers of God' (Jackson 1972).

Since the 1987 seminal work by Kaiser, significant efforts have been made to model the redshift-space large-scale profile of the correlation function and its Fourier counterpart, the power spectrum (e.g. Matsubara 2008; Taruya, Nishimichi & Saito 2010; Reid & White 2011; Seljak & McDonald 2011; Uhlemann, Kopp & Haugg 2015). The standard approach is to use perturbation theory (PT), to compute the density and velocity field to higher order (see e.g. Bernardeau et al. 2002, for a review).

Less explored is the small-scale behaviour of RSD where the density contrast becomes comparable to unity, causing the breakdown of any perturbative-expansion scheme. As a way around this issue, a few alternative approaches have been suggested, spanning from analytic (e.g. Sheth 1996) to hybrid techniques in which *N*-body simulations are used to tune fitting functions (e.g. Tinker 2007; Kwan, Lewis & Linder 2012) or as a reference realization of the redshift-space clustering, in which small departures from the assumed ΛCDM cosmology can be mimicked by varying appropriate halo occupation distribution (HOD) parameters (Reid et al. 2014). A good understanding of this small-scale limit is desirable for two main reasons. (i) It is rich in cosmological information, in particular if our goal is to discriminate between different gravity models. Specifically, it has been shown that modified gravity strongly affects the pairwise velocity dispersion on these scales (Fontanot et al. 2013; Hellwing et al. 2014). (ii) The smaller the separation the higher the signal-to-noise ratio and the less the cosmic variance, i.e. smaller statistical error. Thus, understanding this process allows us to push measurements of the structure growth effects to smaller scales.

With this work, we provide a framework in which these large- and small-scale RSD processes can both be included, so that all

★ E-mail: davide.bianchi@port.ac.uk

© 2016 The Authors
Published by Oxford University Press on behalf of the Royal Astronomical Society

Downloaded from https://academic.oup.com/mnras/article/463/4/3783/2646355 by Divisione Coordinamento Biblioteche Milano user on 09 November 2021

available information can be coherently extracted form redshift surveys. We start from the 'streaming model' (Davis & Peebles 1983; Fisher 1995; Scoccimarro 2004), which describes how the redshift-space correlation function $\xi_S(s_\perp, s_\parallel)$ is modified with respect to its isotropic real-space counterpart $\xi_R(r)$:

$$1+\xi_S(s_\perp, s_\parallel) = \int \mathrm{d}r_\parallel\, [1+\xi_R(r)]\, \mathcal{P}(r_\parallel - s_\parallel|\boldsymbol{r}), \tag{1}$$

where we have ignored wide-angle effects. Here $r^2 = {r_\perp}^2 + {r_\parallel}^2$ and $r_\perp = s_\perp$. The effect of the velocity flows on the observed clustering is encoded in the pairwise line-of-sight velocity distribution function $\mathcal{P}(v_\parallel|\boldsymbol{r}) = \mathcal{P}(r_\parallel - s_\parallel|\boldsymbol{r})$, which has a non-trivial dependence on the separation $\boldsymbol{r}$. Clearly, a proper modelling of this probability distribution function (PDF) is the key ingredient in the description. Starting from this consideration, in Bianchi, Chiesa & Guzzo (2015), hereafter Paper I, we modelled the velocity PDF by introducing the concept of Gaussian Gaussianity (GG), in which the overall PDF is interpreted as a superposition of local Gaussian distributions, whose mean and standard deviation are, in turn, jointly distributed according to a bivariate Gaussian. Here we extend that line of research by introducing the more general concept of Gaussian quasi-Gaussianity (GQG) and making explicit the dependence of the velocity PDF on quantities that can be predicted by theory, namely its first three moments. We do not discuss which theoretical scheme should be preferred for their evaluation, but rather we directly measure these quantities from N-body simulations. Our analysis matches simulations over a large portion of the parameter space, including redshifts from $z = 0$ to 1, dark matter (DM) particles, haloes with mass down to $10^{12}\, h^{-1}\mathrm{M}_\odot$ and scales down to $0\, h^{-1}$ Mpc separation. For all these configurations, we compare the performance of our model with two different implementations of the streaming model: the well-known Gaussian streaming model (GSM), in which a univariate-Gaussian profile is assumed for the velocity PDF (Reid & White 2011); the more recent Edgeworth streaming model (ESM; Uhlemann et al. 2015), in which the skewness is added to this simple Gaussian picture by means of an Edgeworth expansion (see e.g. Blinnikov & Moessner 1998). We show that, under the GQG assumption, a more precise description of the redshift-space clustering is obtained.

This paper is organized as follows. In Section 2, we introduce our model. As this work is the second in a series, the derivation we present follows the 'historical process' that led us to introduce GQG. In Sections 2.1–2.4, we first review how to build a model based on GG, introduced in Paper I, and then show the (unexpected) limitations of such approach. In the remainder of Section 2, we show how to overcome this issue. Our final model is based on a few assumptions, which are referred as ansatze throughout the manuscript. Given this, the model we are proposing should be considered a functional form for the velocity PDF that, irregardless of its derivation, incorporates all the fundamental features observed in both simulations and galaxy surveys, including exponential tails and skewness. If required, this GQG distribution can be exactly shaped into a Gaussian, which means that, by construction, the resulting streaming model is a generalization of the widely used GSM. Furthermore, we show that this PDF has the non-trivial property of being expressible as a functions of its first three moments, thus providing an explicit link to PT. We believe that such a distribution would have been interesting to be studied even if it were unmotivated from a physical point of view, as sometimes happens in the literature. This is of course not the case with GQG, which is explicitly derived based on considerations on how the overall PDF can be decomposed in local PDFs, with the spirit of keeping only the features of these latter that are relevant for RSD. Using N-body simulations as a reference, in Section 3 we compare the performance of our model with that of GSM and ESM. The primary purpose of this comparison is to show that, once the first three moments are given, the remaining degrees of freedom can be effectively absorbed in two numbers, the κ parameters (see Section 2.6). Our results are summarized in Section 4. Details on how we measure physical quantities from the simulations are reported in the appendices. Also in the appendices, we discuss ideas for further developments.

2 MODELLING

2.1 GG distribution

In Paper I, we proposed a functional form for the line-of-sight pairwise velocity distribution,

$$\mathcal{P}(v_\parallel) = \int \mathrm{d}\mu\, \mathrm{d}\sigma\, \mathcal{G}(v_\parallel|\mu,\sigma)\, \mathcal{B}(\mu,\sigma), \tag{2}$$

where

$$\mathcal{G}(v_\parallel|\mu,\sigma) = \frac{1}{\sqrt{2\pi\sigma^2}} \exp\left[-\frac{(v_\parallel-\mu)^2}{2\sigma^2}\right], \tag{3}$$

$$\mathcal{B}(\mu,\sigma) = \frac{1}{2\pi\sqrt{\det(C)}} \exp\left[-\frac{1}{2}\Delta^T C^{-1}\Delta\right], \tag{4}$$

$$\Delta = \begin{pmatrix} \mu - M_\mu \\ \sigma - M_\sigma \end{pmatrix} \qquad C = \begin{pmatrix} C_{\mu\mu} & C_{\mu\sigma} \\ C_{\mu\sigma} & C_{\sigma\sigma} \end{pmatrix}. \tag{5}$$

The interpretation of equation (2) is straightforward: at any given separation $(r_\perp, r_\parallel)$, the overall velocity distribution can be approximated by a superposition of univariate Gaussians whose mean μ and standard deviation σ are, in turn, jointly distributed as a bivariate Gaussian. M_μ and M_σ represent the mean of μ and σ, respectively, whereas C is their covariance matrix. We showed in Paper I that the simple picture in which these univariate Gaussians represent local velocity distributions gives a good match to N-body simulations. Note that hereafter we write $\mathcal{P}(v_\parallel) = \mathcal{P}(v_\parallel|\boldsymbol{r})$, where the dependence on the separation is omitted for brevity, but still present in our model. Specifically, it is encoded in how the parameters $M_\mu = M_\mu(\boldsymbol{r})$, $M_\sigma = M_\sigma(\boldsymbol{r})$ and $C = C(\boldsymbol{r})$ vary with the separation.

Strictly speaking, the above modelling is physically meaningful only if $M_\sigma \gtrsim 3\sqrt{C_{\sigma\sigma}}$, i.e. only if the whole power of the bivariate Gaussian is limited to the positive σ plane. To ensure that the expression is well behaved for $M_\sigma \to 0$, we adopt for $\mathcal{G}$ the normalization factor $\sqrt{2\pi\sigma^2}$ rather than $\sqrt{2\pi}\sigma$, equation (3), and we no longer have to deal with negative local distributions, independently of the width of the bivariate Gaussian $C_{\sigma\sigma}$. We can write

$$\begin{aligned}\mathcal{P}(v_\parallel) &= \int_{-\infty}^{+\infty} \mathrm{d}\mu \left(\int_{-\infty}^{0} \mathrm{d}\sigma\, \mathcal{G}\,\mathcal{B} + \int_{0}^{+\infty} \mathrm{d}\sigma\, \mathcal{G}\,\mathcal{B}\right) \\ &= \int \mathrm{d}\mu\, \mathrm{d}\sigma\, \mathcal{G}(v_\parallel|\mu,\sigma)\, \mathcal{B}^{\pm}(\mu,\sigma),\end{aligned} \tag{6}$$

where we have defined

$$\mathcal{B}^{\pm}(\mu,\sigma) \equiv \begin{cases} \mathcal{B}(\mu,-\sigma) + \mathcal{B}(\mu,\sigma) & \sigma \geq 0 \\ 0 & \sigma < 0 \end{cases}. \tag{7}$$

Equation (6) generalizes equation (2) in a natural way, such that all the fundamental properties of $\mathcal{P}$ are conserved. In particular, the relation between moments of $\mathcal{P}$ and $\mathcal{B}$, presented in the first column of Table 2, remains valid in this more general formulation. Still, it is appropriate to note that the moments of $\mathcal{B}^{\pm}$ differ from those of

Downloaded from https://academic.oup.com/mnras/article/463/4/3783/2646355 by Divisione Coordinamento Biblioteche Milano user on 09 November 2021

Table 1. Definitions and notation adopted to describe the moments of the probability distribution functions considered in this work: $\mathcal{P}$, $\mathcal{B}$ and $\mathcal{B}^{\pm}$. n is the order of the moment and $k \in \{0, 1\}$. Not to overcomplicate the notation, for $\mathcal{B}$ we only define the first non-central and second central moments.

PDF	Moments	Central moments
$\mathcal{P}$	$m^{(n)} \equiv \int \mathrm{d}v_\parallel \; {v_\parallel}^n \; \mathcal{P}(v_\parallel)$	$c^{(n)} \equiv \int \mathrm{d}v_\parallel \; \left[v_\parallel - m^{(1)}\right]^n \; \mathcal{P}(v_\parallel)$
$\mathcal{B}$	$M_\mu \equiv \int \mathrm{d}\mu d\sigma \; \mu \; \mathcal{B}(\mu, \sigma)$	$C_{\mu\mu} \equiv \int \mathrm{d}\mu d\sigma \; (\mu - M_\mu)^2 \; \mathcal{B}(\mu, \sigma)$
	$M_\sigma \equiv \int \mathrm{d}\mu \mathrm{d}\sigma \; \sigma \; \mathcal{B}(\mu, \sigma)$	$C_{\sigma\sigma} \equiv \int \mathrm{d}\mu \mathrm{d}\sigma \; (\sigma - M_\sigma)^2 \; \mathcal{B}(\mu, \sigma)$
		$C_{\mu\sigma} \equiv \int \mathrm{d}\mu \mathrm{d}\sigma \; (\mu - M_\mu)(\sigma - M_\sigma) \; \mathcal{B}(\mu, \sigma)$
$\mathcal{B}^{\pm}$	$M^{(n)}_{k_1,\ldots,k_n} \equiv \int \mathrm{d}\mu \mathrm{d}\sigma \; \mu^{n-\sum_i k_i} \sigma^{\sum_i k_i} \; \mathcal{B}(\mu, \sigma)$	$C^{(n)}_{k_1,\ldots,k_n} \equiv \int \mathrm{d}\mu \mathrm{d}\sigma \; \left[\mu - M_0^{(1)}\right]^{n-\sum_i k_i} \left[\sigma - M_1^{(1)}\right]^{\sum_i k_i} \; \mathcal{B}^{\pm}(\mu, \sigma)$

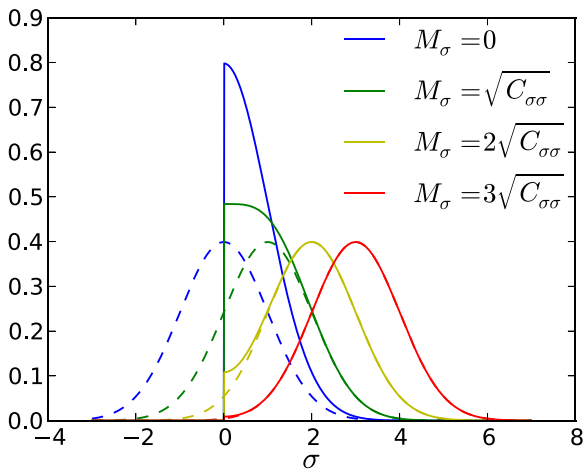

Figure 1. Cuts of $\mathcal{B}$ (dashed) versus cuts of $\mathcal{B}^{\pm}$ (solid) along the μ axis for different values of mean and variance (of σ), M_σ and $C_{\sigma\sigma}$, respectively. For simplicity, we only report the case $M_\mu = C_{\mu\mu} = C_{\mu\sigma} = 0$, but this behaviour is general.

$\mathcal{B}$, and they coincide in the limiting case in which $M_\sigma \gtrsim 3\sqrt{C_{\sigma\sigma}}$.[1] See Table 1 for the definitions of the moments. In Fig. 1, we show the comparison between $\mathcal{B}$ and $\mathcal{B}^{\pm}$ for a few selected cuts in μ.

Although the physical meaning of the GG distribution is well described by equation (6), it is important to note that μ can be integrated analytically. The integration gives

$$\mathcal{P}(v_\parallel) = \int \mathrm{d}\sigma \frac{1}{2\pi\mathcal{A}} \exp\left[-\frac{\sum_{n=0}^{2} \mathcal{K}_n \, (v_\parallel - M_\mu)^n}{2\mathcal{A}^2}\right], \tag{8}$$

where

$$\mathcal{A}^2 = C_{\sigma\sigma}\sigma^2 + C_{\mu\mu}C_{\sigma\sigma} - {C_{\mu\sigma}}^2 \tag{9}$$

$$\mathcal{K}_2 = C_{\sigma\sigma} \tag{10}$$

$$\mathcal{K}_1 = -2C_{\mu\sigma} \, (\sigma - M_\sigma) \tag{11}$$

$$\mathcal{K}_0 = \left(\sigma^2 + C_{\mu\mu}\right) (\sigma - M_\sigma)^2. \tag{12}$$

This result is particularly useful from a numerical point of view since, for any given set of parameters $\{M_\mu, M_\sigma, C_{\mu\mu}, C_{\sigma\sigma}, C_{\mu\sigma}\}$, it allows us to compute $\mathcal{P}$ via a simple, i.e. fast, one-dimensional integration.

Following standard practice, we define the moment generating function (MGF) as

$$\mathcal{M}(t) = \langle e^{t v_\parallel} \rangle = \int d v_\parallel \; e^{t v_\parallel} \; \mathcal{P}(v_\parallel). \tag{13}$$

One important property of the MGF is that it allows us to compute the moments iteratively at any order,

$$m^{(n)} = \left.\frac{\mathrm{d}^n \mathcal{M}}{\mathrm{d}t^n}\right|_{t=0}. \tag{14}$$

For the GG distribution we get

$$\mathcal{M}(t) = \frac{1}{\sqrt{1 - t^2 C_{\sigma\sigma}}} \exp\left[t M_\mu + \frac{1}{2} t^2 {M_\sigma}^2 + \Theta(t)\right], \tag{15}$$

where

$$\Theta(t) = \frac{1/2}{1 - t^2 C_{\sigma\sigma}} \left[t^2 C_{\mu\mu} + 2t^3 C_{\mu\sigma} M_\sigma + t^4 \left({M_\sigma}^2 C_{\sigma\sigma} - \det C\right)\right]. \tag{16}$$

Similarly, we can define the cumulant generating function, $\mathcal{C}(t) = \log\langle e^{t v_\parallel} \rangle$, which, for the GG distribution, takes the form

$$\mathcal{C}(t) = t M_\mu + \frac{1}{2} t^2 {M_\sigma}^2 + \Theta(t) - \frac{1}{2} \ln\left(1 - t^2 C_{\sigma\sigma}\right). \tag{17}$$

In the following, we briefly discuss a few cases of interest corresponding to particular combinations of the parameters of the bivariate Gaussian.

(i) If $C_{\sigma\sigma} = C_{\mu\sigma} = 0$ we get

$$\mathcal{M}(t) = \exp\left[t M_\mu + \frac{1}{2} t^2 \left({M_\sigma}^2 + C_{\mu\mu}\right)\right], \tag{18}$$

which is the MGF of a Gaussian with mean M_μ and variance ${M_\sigma}^2 + C_{\mu\mu}$. In other words, the superposition of fixed-variance Gaussians (i.e. $C_{\sigma\sigma} = 0$) is, in turn, a Gaussian. We now consider the two limiting cases, $C_{\mu\mu} = 0$ and $M_\sigma = 0$. From a physical point of view, $C_{\mu\mu} = 0$ corresponds to a scenario in which at any position in the Universe we measure the same pairwise velocity PDF,

[1] Following the notation introduced in Table 1, when $M_\sigma \lesssim 3\sqrt{C_{\sigma\sigma}}$, for the first non-central moments it holds that

$$M_0^{(1)} = M_\mu \qquad M_1^{(1)} \neq M_\sigma,$$

whilst for the second central moments,

$$C_{00}^{(2)} = C_{\mu\mu} \qquad C_{11}^{(2)} \neq C_{\sigma\sigma} \qquad C_{01}^{(2)} \neq C_{\mu\sigma}.$$

More in general, $\mathcal{B}$ and $\mathcal{B}^{\pm}$ share by construction all the even non-central moments $M^{(2n)}_{k_1,\ldots,k_{2n}}$.

Downloaded from https://academic.oup.com/mnras/article/463/4/3783/2646355 by Divisione Coordinamento Biblioteche Milano user on 09 November 2021

Table 2. Moments of the line-of-sight velocity distribution $\mathcal{P}$ as a function of the moments of the bivariate Gaussian $\mathcal{B}$ (left-hand column) and vice versa (right-hand column).

$\mathcal{P}$ versus $\mathcal{B}$	$\mathcal{B}$ versus $\mathcal{P}$
$m^{(1)} = M_\mu$	$M_\mu = m^{(1)}$
$c^{(2)} = {M_\sigma}^2 + C_{\mu\mu} + C_{\sigma\sigma}$	$C_{\sigma\sigma} = \frac{1}{20}\frac{c^{(5)}}{c^{(3)}} - \frac{1}{2}c^{(2)}$
$c^{(3)} = 6M_\sigma C_{\mu\sigma}$	${M_\sigma}^2 = \frac{c^{(4)} - 3c^{(2)2} - 6{C_{\sigma\sigma}}^2 + \sqrt{\left[c^{(4)} - 3c^{(2)2} - 6{C_{\sigma\sigma}}^2\right]^2 - 16C_{\sigma\sigma}c^{(3)2}}}{24C_{\sigma\sigma}}$
$c^{(4)} = 3({M_\sigma}^2 + C_{\mu\mu})^2 + 6\left[C_{\sigma\sigma}\left(3{M_\sigma}^2 + C_{\mu\mu}\right) + 2{C_{\mu\sigma}}^2\right] + 9{C_{\sigma\sigma}}^2$	$C_{\mu\mu} = c^{(2)} - {M_\sigma}^2 - C_{\sigma\sigma}$
$c^{(5)} = 60M_\sigma C_{\mu\sigma}({M_\sigma}^2 + C_{\mu\mu} + 3C_{\sigma\sigma})$	$C_{\mu\sigma} = \frac{1}{6}\frac{c^{(3)}}{M_\sigma}$

which is clearly what we expect in the large-scale limit.[2] On the other hand, the limit $M_\sigma = 0$ represents a superposition of Dirac deltas whose mean is Gaussian distributed. Such a scenario is not compatible with any reasonable pairwise velocity PDF, although it might be useful for different applications, e.g. when describing the time evolution of the 1-particle velocity PDF. More explicitly, in the phase-space formalism, it is commonly assumed that, at any position, the 1-particle velocity density (more precisely the momentum density) is well approximated by a Dirac delta (the so-called single-flow approximation). After shell crossing this assumption is no longer valid and we have to resort to distributions with a broader profile, e.g. Gaussians. Whether the evolution of these distributions can be captured by a bivariate Gaussian description of their mean and variance, or, in other words whether the statistics of a fluid can be described by a GG distribution is an interesting question that we will try to answer in a further work.

(ii) In the very small-scale limit the statistics are dominated by virialized regions, which implies negligible local infall velocity, i.e. $M_\mu = C_{\mu\mu} = C_{\mu\sigma} = 0$. The corresponding MGF is

$$\mathcal{M}(t) = \frac{1}{\sqrt{1 - t^2 C_{\sigma\sigma}}} \exp\left(\frac{\frac{1}{2}t^2 {M_\sigma}^2}{1 - t^2 C_{\sigma\sigma}}\right). \tag{19}$$

As shown in appendix B, when ${M_\sigma}^2 = 2C_{\sigma\sigma}$ this latter approximate the MGF of an exponential distribution. It is well known from simulations and observations (e.g. Davis & Peebles 1983; Zurek et al. 1994) that the small-scale velocity PDF is nearly exponential and is therefore important that this limit is included in our description, although we will not explicitly use it in our modelling (but see Appendix D).

Finally, it is worth mentioning two potentially relevant applications of the GG-distribution MGF.

(i) It can be used to compute the velocity PDF via a simple fast Fourier transform, which is computationally attractive.

(ii) It allows us to directly model the redshift-space power spectrum, see e.g. equation (13) in Scoccimarro (2004).

2.2 Strategy

If we assume that the true velocity PDF is well approximated by the GG distribution, equation (2), or equivalently equation (6), we can think of using this model to extract cosmological information from galaxy redshift surveys via RSD.

Since the five scale-dependent parameters M_μ, M_σ, $C_{\mu\mu}$, $C_{\sigma\sigma}$ and $C_{\mu\sigma}$ on which the distribution depends have a clear interpretation, we can think of directly predicting them. One intriguing aspect of such an approach is that it allows us to reason in terms of local distributions, suggesting the possibility of naturally including a multi-stream description. In general, such an issue is expected to become more and more important as we want to describe the small-scale non-linear regime. Roughly speaking, an extension form single- to multiflow scenario could be obtained by using Gaussians instead of Dirac delta distributions for the local 1-particle velocity PDF (more properly for the momentum part of the phase-space distribution function). The resulting local pairwise velocity distribution will then be Gaussian as well and, as a consequence, the overall pairwise velocity PDF will be compatible with the GG prescription. We leave these considerations to further work.

Instead, we follow the conceptual spirt of the GSM, as implemented by Reid & White (2011). The GSM relies on the assumption that, at any given separation $(r_\perp, r_\parallel)$, the overall line-of-sight pairwise velocity PDF is well approximated by an univariate Gaussian, whose mean and variance were obtained by Reid & White (2011) via PT. This approach can be extended to include more general and realistic distributions, with more than two free moments. The nth moment of the line-of sight pairwise velocity distribution $\mathcal{P}(v_\parallel)$ is

$$m^{(n)} = \frac{\left\langle (1+\delta_1)(1+\delta_2)\, {v_\parallel}^n \right\rangle}{\langle (1+\delta_1)(1+\delta_2) \rangle}, \tag{20}$$

where $\delta_i = \delta(\boldsymbol{x}_i)$, with δ being the usual density contrast. Similarly, the central moments are defined as

$$c^{(n)} = \frac{\left\langle (1+\delta_1)(1+\delta_2)\left(v_\parallel - m^{(1)}\right)^n \right\rangle}{\langle (1+\delta_1)(1+\delta_2) \rangle}. \tag{21}$$

In principle, these quantities can be predicted by PT even for $n > 2$ (e.g. Juszkiewicz, Fisher & Szapudi 1998; Uhlemann et al. 2015, see also Appendix D for a simple example of how these moments can be predicted on nonlinear scales). The GG distribution includes the Gaussian distribution as a limiting case.

By inverting the system in the left-hand column of Table 2 we can write the bivariate Gaussian $\mathcal{B}$ as a function of the first five moments of $\mathcal{P}(v_\parallel)$, namely $m^{(1)}$, $c^{(2)}$, $c^{(3)}$, $c^{(4)}$ and $c^{(5)}$. Explicit expressions for the resulting M_μ, M_σ, $C_{\mu\mu}$, $C_{\sigma\sigma}$ and $C_{\mu\sigma}$ are reported in the right-hand column of Table 2. The inversion is well defined as long as $c^{(3)} \neq 0$. Formally, if $c^{(3)} = 0$ (which implies that all the odd central moments disappear as well), in order to have a one-to-one correspondence between $\mathcal{P}$ and $\mathcal{B}$ we need to include the sixth moment in the analysis. We will see that this is not relevant in our modelling.

[2] In this description, the PDF is Gaussian because we are using local Gaussians as building blocks (in the following this assumption will be slightly relaxed). As discussed in Section 2.6, even on large scales the true velocity PDF is never exactly Gaussian. None the less, the Gaussian approximation becomes more and more accurate as the separation increases. In practice, we will use this limit as an 'infinite-scale' limit, which is never really reached.

Downloaded from https://academic.oup.com/mnras/article/463/4/3783/2646355 by Divisione Coordinamento Biblioteche Milano user on 09 November 2021

Although in principle the first five moments can be obtained via PT, in practice the complexity of the calculations grows rapidly with the order of both moment and perturbative expansion. We therefore decide to adopt an hybrid approach in which we assume that the first three moments can be directly predicted, whilst fourth and fifth moment (and in general all higher order moments) are implicitly modelled as functions of a set of physically meaningful dimensionless parameters, which arise naturally by general considerations about the properties of the GG distribution itself. The amplitude of these parameters is then obtained by comparisons with *N*-body simulations.

2.3 Parametrization

The expression for the first three moments of $\mathcal{P}$ as a function of the moments of $\mathcal{B}$ is

$$m^{(1)} = M_\mu \tag{22}$$

$$c^{(2)} = {M_\sigma}^2 + C_{\mu\mu} + C_{\sigma\sigma} \tag{23}$$

$$c^{(3)} = 6 M_\sigma C_{\mu\sigma}. \tag{24}$$

It is clear that the GG parameters $\{M_\mu, M_\sigma, C_{\mu\mu}, C_{\sigma\sigma}, C_{\mu\sigma}\}$ are uniquely defined once we specify $\{m^{(1)}, c^{(2)}, c^{(3)}\}$ plus a prescription on how to split $c^{(2)}$ into the three summands ${M_\sigma}^2$, $C_{\mu\mu}$ and $C_{\sigma\sigma}$, i.e. a prescription for their relative weight. We then rewrite equation (23) in terms of three dimensionless quantities,

$$1 = \frac{{M_\sigma}^2}{c^{(2)}} + \frac{C_{\mu\mu}}{c^{(2)}} + \frac{C_{\sigma\sigma}}{c^{(2)}} = \varphi_{M\sigma} + \varphi_{C\mu\mu} + \varphi_{C\sigma\sigma}. \tag{25}$$

Due to isotropy, $\mathcal{P}(v_\parallel | r_\perp, r_\parallel)$ can be seen as the projection of a two-dimensional distribution $\mathcal{P}_r(v_r, v_t | r)$, where the subscripts r and t stand for parallel and perpendicular to the pair separation, see Appendix A. As a consequence $c^{(2)}$ is in general characterized by the following symmetry,

$$c^{(2)}(r, \mu_\theta) = c_r^{(2)}(r)\, \mu_\theta^2 + c_t^{(2)}(r)\, \left(1 - \mu_\theta^2\right). \tag{26}$$

It is then convenient to define

$$1 = \varphi_{M\sigma}^{(r)}(r) + \varphi_{C\mu\mu}^{(r)}(r) + \varphi_{C\sigma\sigma}^{(r)}(r) \tag{27}$$

$$1 = \varphi_{M\sigma}^{(t)}(r) + \varphi_{C\mu\mu}^{(t)}(r) + \varphi_{C\sigma\sigma}^{(t)}(r) \tag{28}$$

so that instead of three two-dimensional functions we have to deal with six one-dimensional functions.[3]

Clearly, given the above equations, the functions we need to model are actually only four. A simple ansatz is then

$$\varphi_{C\mu\mu}^{(r)}(r) = \kappa_\mu^{(r)}\, g(r/r_g) \tag{29}$$

$$\varphi_{C\sigma\sigma}^{(r)}(r) = \kappa_\sigma^{(r)}\, g(r/r_g) \tag{30}$$

$$\varphi_{M\sigma}^{(r)}(r) = 1 - \varphi_{C\mu\mu}^{(r)}(r) - \varphi_{C\sigma\sigma}^{(r)}(r) \tag{31}$$

$$\varphi_{C\mu\mu}^{(t)}(r) = \kappa_\mu^{(t)}\, g(r/r_g) \tag{32}$$

$$\varphi_{C\sigma\sigma}^{(t)}(r) = \kappa_\sigma^{(t)}\, g(r/r_g) \tag{33}$$

$$\varphi_{M\sigma}^{(t)}(r) = 1 - \varphi_{C\mu\mu}^{(t)}(r) - \varphi_{C\sigma\sigma}^{(t)}(r), \tag{34}$$

where g can be any monotonic regular function such that

$$g(r) \to \begin{cases} 0 & r \to \infty \\ 1 & r \to 0 \end{cases}, \tag{35}$$

e.g. $g(r/r_g) = \frac{1}{1+(r/r_g)^2}$. By construction r_g represents the scale above which the Gaussian limit is recovered, whereas $\kappa_\mu^{(r)}$, $\kappa_\sigma^{(r)}$, $\kappa_\mu^{(t)}$, $\kappa_\sigma^{(t)}$ represent the amplitudes of the corresponding φ functions at $r = 0$.

2.4 The skewness problem

Independently of the functional form chosen for $\varphi_{M\sigma}$, $\varphi_{C\mu\mu}$ and $\varphi_{C\sigma\sigma}$, from equations (24) and (25) we can write

$$c^{(3)} = 6 {c^{(2)}}^{3/2} \rho \sqrt{\varphi_{M\sigma}\, \varphi_{C\mu\mu}\, \varphi_{C\sigma\sigma}}, \tag{36}$$

where $\rho \equiv C_{\mu\sigma}/\sqrt{C_{\mu\mu}\, C_{\sigma\sigma}}$ is the correlation coefficient of the bivariate Gaussian. Since in general $|\rho| < 1$, for any given $c^{(2)}$ equation (36) provides us with an upper bound for $|c^{(3)}|$,

$$\left|c^{(3)}\right| < \frac{2}{\sqrt{3}} {c^{(2)}}^{3/2}, \tag{37}$$

corresponding to $\rho = \pm 1$ and $\varphi_{M\sigma} = \varphi_{C\mu\mu} = \varphi_{C\sigma\sigma} = 1/3$. By explicitly defining the skewness, $\gamma \equiv c^{(3)}/{c^{(2)}}^{3/2}$, we have $|\gamma| < 2/\sqrt{3} \sim 1.155$. In Fig. 2, we show that this limit is reached for DM at $z = 0$ at $r \sim 5\, h^{-1}$ Mpc, $\mu_\theta \sim 0$, and is exceeded at higher redshift. For halo catalogues, not shown in the figure for simplicity, this behaviour is even more marked.[4] Thus, we see that the GG model is unable to match the observed level of skewness and requires further generalization as described in the next section (but see also Appendix C for an alternative approach).

2.5 Gaussian (local) quasi-Gaussianity

To overcome this problem, we generalize GG by introducing the concept of Gaussian (local) quasi-Gaussianity (GQG). We can account for a small deviation from local Gaussianity by Edgeworth-expanding the local distributions,

$$\mathcal{P}(v_\parallel) = \int \mathrm{d}\mu\, \mathrm{d}\sigma\, \mathcal{E}(v_\parallel | \mu, \sigma)\, \mathcal{B}(\mu, \sigma), \tag{38}$$

where

$$\mathcal{E}(v_\parallel | \mu, \sigma) = \mathcal{G}(v_\parallel | \mu, \sigma) \left[1 + \frac{\gamma_L}{6}\, H_3\left(\frac{v_\parallel - \mu}{\sigma}\right)\right], \tag{39}$$

$$\gamma_L = \frac{c_L^{(3)}}{\sigma^3}, \tag{40}$$

$$H_3(x) = x^3 - 3x. \tag{41}$$

$c_L^{(3)}$ is third central moment of the local distribution $\mathcal{E}$ (hence γ_L is the local skewness) and H_3 is the third probabilistic Hermite polynomials. It should be noted that, since the integral in equation (38) formally includes negative values of σ, from equations (39) and (41) it follows that both positively and negatively skewed (quasi)

[3] This decomposition is based on the implicit assumption that the symmetry described by equation (26) can be applied not only to $c^{(2)}$ but also individually to each of its three building blocks, i.e. $C_{\sigma\sigma}(r, \mu_\theta) = C_{\sigma\sigma}^{(r)}(r)\mu_\theta^2 + C_{\sigma\sigma}^{(t)}(r)\left(1 - \mu_\theta^2\right)$, and similarly for ${M_\sigma}^2$ and $C_{\mu\mu}$. The φ functions can be explicitly defined as $\varphi_{C\sigma\sigma}^{(r)} = C_{\sigma\sigma}^{(r)}/c_r^{(2)}$ and $\varphi_{C\sigma\sigma}^{(t)} = C_{\sigma\sigma}^{(t)}/c_t^{(2)}$. It follows that $\varphi_{C\sigma\sigma} = \varphi_{C\sigma\sigma}^{(r)}\mu_\theta^2 + \varphi_{C\sigma\sigma}^{(t)}\left(1 - \mu_\theta^2\right)$.

[4] In Paper I this issue did not arise because only DM particles at $z = 0$ were considered.

Downloaded from https://academic.oup.com/mnras/article/463/4/3783/2646355 by Divisione Coordinamento Biblioteche Milano user on 09 November 2021

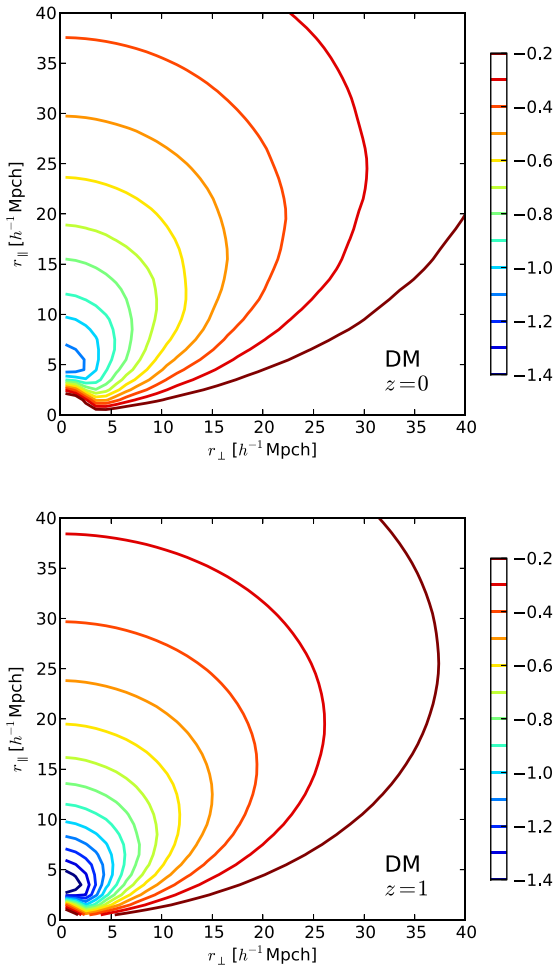

Figure 2. Measurement from simulations of the skewness of the line-of-sight pairwise velocity distribution, $\gamma = c^{(3)}/c^{(2)3/2}$, presented using iso-skewness contours as a function of the real-space separation parallel and perpendicular to the line of sight, $r_\parallel$ and $r_\perp$, respectively, for DM particles from the MDR1 simulation at two different redshifts, as labelled in the figure.

Gaussians contribute to the overall PDF. This guaranties that the net contribution of the local to the overall skewness vanishes for $\sigma \to 0$, a desirable property if we want to avoid the nonsense of skewed Dirac deltas. It is none the less useful to say that, although the formulation of GQG clearly follows from the idea of allowing for a small skewness correction on local distributions, in a more general picture it can also be seen just as a generalized Edgeworth expansion, i.e. a practical way to control the skewness of a distribution without changing its first two moments. In the perspective of using the model for a Monte Carlo estimation of cosmological parameters in which second and third moments are free to vary, it is important to have removed a potential source of artefacts such those that would arise from exceeding the upper limit of equation (37). As in the simpler case of the GG distribution, it is possible to integrate equation (38) with respect to μ,

$$\mathcal{P}(v_\parallel) = \int \mathrm{d}\sigma \left\{ \frac{1}{2\pi\mathcal{A}} \exp\left[-\frac{\sum_{n=0}^{2} \mathcal{K}_n\,(v_\parallel - M_\mu)^n}{2\mathcal{A}^2} \right] \times \left[1 + \frac{\mathcal{S}}{\mathcal{A}^6} \sum_{k=0}^{3} \mathcal{Q}_k\,(v_\parallel - M_\mu)^k \right] \right\}, \tag{42}$$

where $\mathcal{A}$ and $\mathcal{K}_n$ are defined in Section 2.1, and

$$\mathcal{S} = \gamma_L\,\sigma^3/6 \tag{43}$$

$$\mathcal{Q}_3 = {C_{\sigma\sigma}}^3 \tag{44}$$

$$\mathcal{Q}_2 = -3C_{\mu\sigma}{C_{\sigma\sigma}}^2\,(\sigma - M_\sigma) \tag{45}$$

$$\mathcal{Q}_1 = 3C_{\sigma\sigma}[M_\sigma {C_{\mu\sigma}}^2 (M_\sigma - 2\sigma) + {C_{\mu\sigma}}^2(\sigma^2 + C_{\sigma\sigma}) - {C_{\sigma\sigma}}^2(\sigma^2 + C_{\mu\mu})] \tag{46}$$

$$\mathcal{Q}_0 = {C_{\mu\sigma}}^3[3C_{\sigma\sigma}(M_\sigma - \sigma) - (\sigma - M_\sigma)^3] + 3C_{\mu\sigma}{C_{\sigma\sigma}}^2(\sigma^2 + C_{\mu\mu})(\sigma - M_\sigma). \tag{47}$$

The first three moments of the GQG distribution are

$$m^{(1)} = M_\mu \tag{48}$$

$$c^{(2)} = {M_\sigma}^2 + C_{\mu\mu} + C_{\sigma\sigma} \tag{49}$$

$$c^{(3)} = 6M_\sigma C_{\mu\sigma} + \gamma_L M_\sigma({M_\sigma}^2 + 3C_{\sigma\sigma}). \tag{50}$$

These are the same as the GG distribution apart for the $\gamma_L M_\sigma({M_\sigma}^2 + 3C_{\sigma\sigma})$ term which accounts for the excess skewness. Keeping in mind that $c^{(3)}$ is given and that equation (50) can be written as $c^{(3)} = 6\rho\sqrt{{M_\sigma}^2 C_{\mu\mu}C_{\sigma\sigma}} + \gamma_L M_\sigma({M_\sigma}^2 + 3C_{\sigma\sigma})$, there are (at least) two practical ways to use the GQG prescription.

(i) We can define

$$\rho_0 = \frac{c^{(3)}}{6\sqrt{{M_\sigma}^2 C_{\mu\mu}C_{\sigma\sigma}}}, \tag{51}$$

and adopt the following prescription,

$$\begin{bmatrix} \rho \\ \gamma_L \end{bmatrix} = \begin{bmatrix} \rho_0 \\ 0 \end{bmatrix}, \tag{52}$$

if $|\rho_0| < 1$, whilst

$$\begin{bmatrix} \rho \\ \gamma_L \end{bmatrix} = \begin{bmatrix} \rho_0/|\rho_0| \\ \frac{c^{(3)} - \rho_0/|\rho_0|\,6\sqrt{{M_\sigma}^2 C_{\mu\mu}C_{\sigma\sigma}}}{M_\sigma({M_\sigma}^2 + 3C_{\sigma\sigma})} \end{bmatrix}, \tag{53}$$

elsewhere. This corresponds to using GQG as an empirical correction for GG, to be 'switched on' only when required by the third moment. The benefit of this approach is that it does not require any additional parameter,[5] the downside is that is not guaranteed that the shape of the velocity PDF varies smoothly with $(r_\perp, r_\parallel)$.

(ii) The alternative is to use

$$\begin{bmatrix} \rho \\ \gamma_L \end{bmatrix} = \begin{bmatrix} \alpha\,\frac{c^{(3)}}{6\sqrt{{M_\sigma}^2 C_{\mu\mu}C_{\sigma\sigma}}} \\ (1-\alpha)\,\frac{c^{(3)}}{M_\sigma({M_\sigma}^2 + 3C_{\sigma\sigma})} \end{bmatrix}, \tag{54}$$

where, by construction, $\alpha \in (0, 1)$ controls the ratio between the skewness created by the covariance $C_{\mu\sigma}$ and the local skewness.

[5] Formally for $|\rho| = 1$ a bivariate Gaussian is not well defined, therefore for any practical application we have to modify equation (53) with $\rho = \frac{\rho_0}{|\rho_0|} - \epsilon$, where $\epsilon \ll 1$.

Downloaded from https://academic.oup.com/mnras/article/463/4/3783/2646355 by Divisione Coordinamento Biblioteche Milano user on 09 November 2021

In practice, rather then α we prefer to use the parameter $\tau \in (0, +\infty)$, defined as follows,

$$\alpha = \left(\varphi^{(r)}_{C\mu\mu}\, \varphi^{(r)}_{C\sigma\sigma}\right)^{\tau}, \tag{55}$$

which is just a simple power-law ansatz, guaranteeing that when $\varphi^{(r)}_{C\mu\mu} = 0$ or $\varphi^{(r)}_{C\sigma\sigma} = 0$ the global skewness comes from the local one alone, i.e. $\alpha = 0$, without introducing further parameters. This is somehow required by the fact that when $\varphi^{(r)}_{C\mu\mu} = 0$ or $\varphi^{(r)}_{C\sigma\sigma} = 0$ the covariance is not well defined.[6] The same argument does not apply for $\varphi^{(t)}_{C\mu\mu}$ and $\varphi^{(t)}_{C\sigma\sigma}$ because, for $\mu_\theta = 0$, the skewness disappears by symmetry. Clearly, in terms of pros and cons, this second approach is exactly the opposite of the first one.

Having tested both of the above solutions, we implement approach (ii). The reason behind this choice is that the profile of the redshift-space correlation function obtained via approach (i) is affected by the presence of wiggles on small scales, which might induce an artificial scale dependence, e.g. when fitting for cosmological parameters. Likely, these undesired features are a direct consequence of the non-smooth behaviour discussed above. As for the amplitude of the local skewness, we can roughly estimate $\gamma_L \in (-0.3, 0)$. Note, however, that this is an indirect measurement, obtained by assuming the model introduced in Section 2.6, and as such it should be intended as a consistency test to ensure that the deviations from local Gaussianity are not too large.

2.6 Simplest possible ansatz

For a model to be useful it is important to keep it as simple as possible (but no simpler). With this in mind, we discuss here the simplest possible ansatz for the parameters $\kappa^{(r)}_\mu$, $\kappa^{(r)}_\sigma$, $\kappa^{(t)}_\mu$, $\kappa^{(t)}_\sigma$, r_g and τ.

(i) Although the univariate-Gaussian assumption has been proved successful in describing the large scale behaviour of massive haloes from *N*-body simulations, we know that the true velocity PDF never really reaches the Gaussian limit (e.g. Scoccimarro 2004). In fact, even in linear theory, the multivariate Gaussian joint distribution of density and velocity field does not yield a Gaussian line-of-sight pairwise velocity PDF (Fisher 1995). Furthermore, we expect the higher order moments of the velocity PDF to become important only on relatively small scales where the correlation function is steeper, see e.g. equation 15 in Paper I, or, in other words, we expect the shape of the velocity PDF not to be particularly relevant on large scales. This suggest that we adopt $r_g = +\infty$.

(ii) A relevant part of the global skewness is due to the covariance $C_{\mu\sigma}$ between local infall and velocity dispersion (Paper I and Tinker 2007). We have just shown that, when GG is assumed, the maximum efficiency in converting the covariance into skewness is obtained for $\varphi_{C\mu\mu} = \varphi_{C\sigma\sigma} = 1/3$. In general, the skewness reaches its maximum for $\mu_\theta = 1$ and disappears for $\mu_\theta = 0$. This suggests that we adopt $\kappa^{(r)}_\mu = \kappa^{(r)}_\sigma = 1/3$.

(iii) Similarly, the value of τ must be small enough to be compatible with the general picture in which the skewness is largely sourced by the covariance. On the other hand, it cannot be zero because of the skewness problem described in Section 2.4. Based on our measurements, in the most extreme cases, corresponding to high-redshift DM and low-redshift small-mass haloes, the skewness can exceed the upper limit given by GG of ∼40 per cent. From equations (54) and (55), it is easy to see that this missing skewness can be obtained by setting[7] $\tau = 1/4$.

With these ansatze, our model only depends on the first three moments of the velocity PDF, $m^{(1)}$, $c^{(2)}$ and $c^{(3)}$, plus two free parameters, $\kappa^{(t)}_\mu$, $\kappa^{(t)}_\sigma$. We show in Section 3 that this model gives a good description of the redshift-space clustering. It should none the less be said that, if we are interested in the true shape of the velocity PDF, e.g. when dealing with direct measurements of the velocity field (e.g. Springob et al. 2007; Tully et al. 2013), the above assumptions should be relaxed.

2.7 Model

We provide a brief summary of our methodology for modelling the redshift-space clustering:

(i) The first three velocity moments can be decomposed in radial and tangential components $m^{(1)}_r$, $c^{(2)}_r$, $c^{(2)}_t$, $c^{(3)}_r$ and $c^{(3)}_t$, which depend on the real-space separation r, but not on μ_θ, see Appendix A. We assume that these quantities can be predicted theoretically as a function of cosmological parameters.

(ii) We evaluate the scale-dependent GQG parameters as

$$M_\mu = m^{(1)}_r(r)\, \mu_\theta \tag{56}$$

$$C_{\mu\mu} = \frac{1}{3} c^{(2)}_r(r)\, \mu^2_\theta + \kappa^{(t)}_\mu c^{(2)}_t(r)\, \left(1 - \mu^2_\theta\right) \tag{57}$$

$$C_{\sigma\sigma} = \frac{1}{3} c^{(2)}_r(r)\, \mu^2_\theta + \kappa^{(t)}_\sigma c^{(2)}_t(r)\, \left(1 - \mu^2_\theta\right) \tag{58}$$

$$M_\sigma{}^2 = c^{(2)}_r(r)\, \mu^2_\theta + c^{(2)}_t(r)\, \left(1 - \mu^2_\theta\right) - C_{\mu\mu} - C_{\sigma\sigma} \tag{59}$$

$$C_{\mu\sigma} = \frac{1}{\sqrt{3}} \frac{\left[c^{(3)}_r(r)\, \mu^2_\theta + c^{(3)}_t(r)\, \left(1 - \mu^2_\theta\right)\right] \mu_\theta}{6 M_\sigma} \tag{60}$$

$$\gamma_L = \left(1 - \frac{1}{\sqrt{3}}\right) \frac{\left[c^{(3)}_r(r)\, \mu^2_\theta + c^{(3)}_t(r)\, \left(1 - \mu^2_\theta\right)\right] \mu_\theta}{M_\sigma (M_\sigma{}^2 + 3 C_{\sigma\sigma})}, \tag{61}$$

where $\kappa^{(t)}_\mu, \kappa^{(t)}_\sigma \in (0, 1)$, with $\kappa^{(t)}_\mu + \kappa^{(t)}_\sigma \leq 1$, are scale-independent dimensionless parameters, which, in the simplest scenario, can be used as nuisance parameters or tuned to simulations.

(iii) We use the GQG parameters to compute the scale-dependent velocity distribution, $\mathcal{P}$, via equation (42). The procedure is self-consistent, i.e. the second moment of the so obtained distribution is exactly $c^{(2)} = c^{(2)}_r(r)\, \mu^2_\theta + c^{(2)}_t(r)\, \left(1 - \mu^2_\theta\right)$, regardless of the amplitude of $\kappa^{(t)}_\mu$ and $\kappa^{(t)}_\sigma$, and similarly for $m^{(1)}$ and $c^{(3)}$.

(iv) We use $\mathcal{P}$ and the real-space correlation function ξ_R to obtain the redshift-space correlation function ξ_S via equation (1), where ξ_R is assumed to be predicted by theory or measured from data (e.g. Saunders, Rowan-Robinson & Lawrence 1992).

[6] In general, equation (55) would require more investigation but, in practice, hereafter we model $\varphi^{(r)}_{C\mu\mu}$ and $\varphi^{(r)}_{C\sigma\sigma}$ as constant functions and the relation between α and τ becomes trivial.

[7] In this final model, $\tau = 1/4$ corresponds to $\alpha \sim 0.6$. As a reference, $\tau = 0$ corresponds to $\alpha = 1$ (i.e. GG is recovered), whereas $\tau > 1$ corresponds to $\alpha \sim 0$ (i.e. the global skewness is sourced by the local skewness alone). We tested the performance of the model for $0.4 \lesssim \alpha \lesssim 0.8$, and we concluded that, within this range, variations in α can be effectively absorbed in small changes of the free parameters $\kappa^{(t)}_\mu$ and $\kappa^{(r)}_\sigma$.

Downloaded from https://academic.oup.com/mnras/article/463/4/3783/2646355 by Divisione Coordinamento Biblioteche Milano user on 09 November 2021

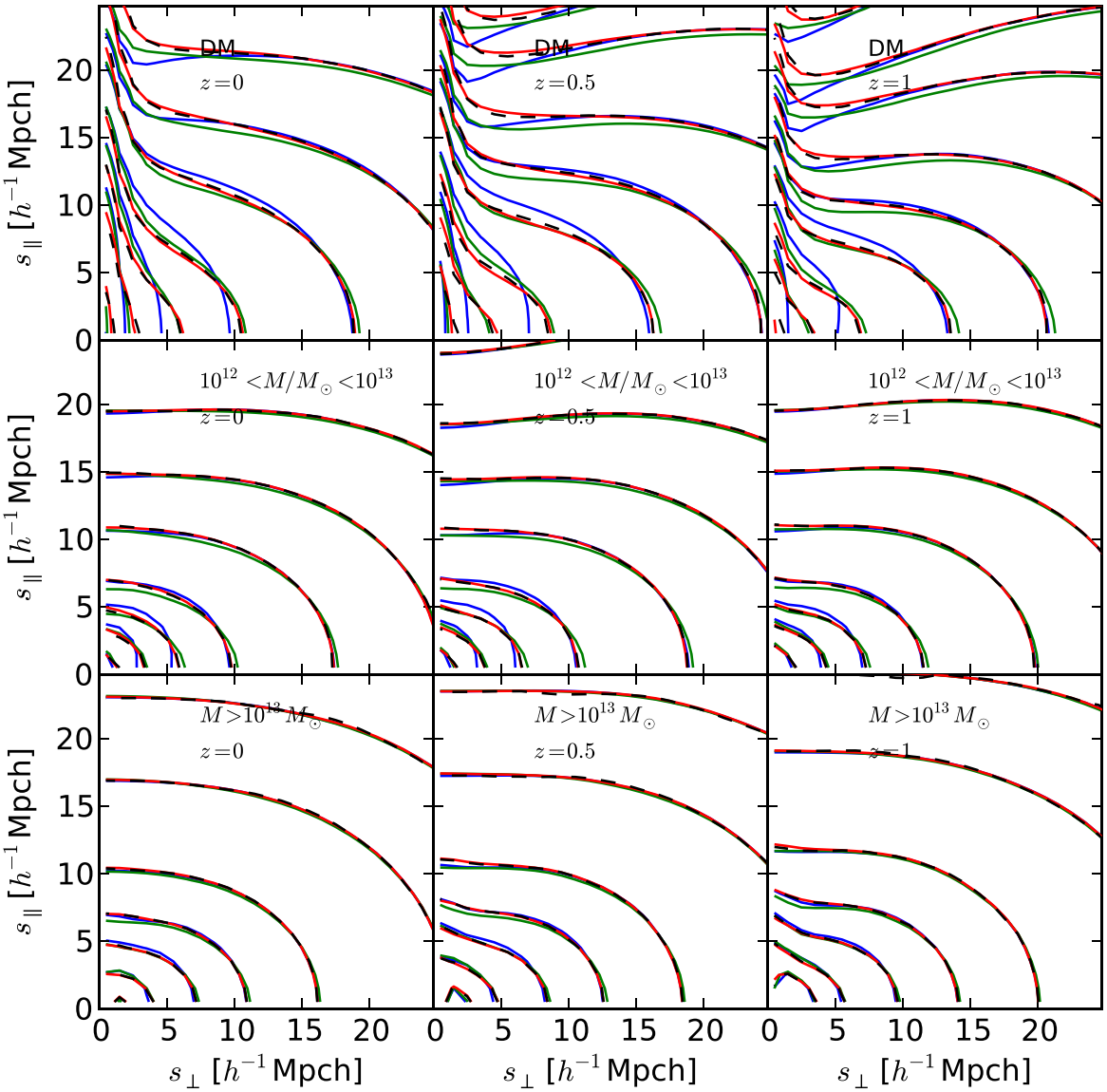

Figure 3. Redshift-space correlation function as a function of the redshift-space separation parallel and perpendicular to the line of sight, $s_\parallel$ and $s_\perp$, respectively, for different tracers and redshifts as labelled in the figure. The iso-correlation contours are obtained via the streaming model with different assumptions for the line-of-sight velocity PDF, specifically: direct measure from the simulations, black dashed; direct measure of the first three moments from the simulations plus GQG assumption, red solid; direct measure of the first three moments from the simulations plus Edgeworth expansion, blue solid; direct measure of the first two moments from the simulations plus univariate Gaussian assumption, green solid.

The above equations refer to the 'simplest possible ansatz' discussed in Section 2.6, but the generalization to a more complex scenario is straightforward.

3 COMPARISON WITH SIMULATIONS

For our investigation we use the data from the MultiDark MDR1 run (Prada et al. 2012), which follows the dynamics of 2048^3 particles over a cubical volume of $(1000\,h^{-1}\mathrm{Mpc})^3$. The set of cosmological parameters assumed for this simulation is compatible with *WMAP5* and *WMAP7* data, $\{\Omega_\mathrm{m}, \Omega_\Lambda, \Omega_\mathrm{b}, \sigma_8, n_\mathrm{s}\} = \{0.27, 0.73, 0.047, 0.82, 0.95\}$. We consider three different redshifts, $z = 0$, 0.5 and 1. For each redshift, we consider DM particles and two mass-selected halo catalogues, $10^{12} < (M/\mathrm{M}_\odot) < 10^{13}$ and $M > 10^{13}\,\mathrm{M}_\odot$. The haloes are identified via a friend-of-friend algorithm, with linking length 0.17.

Since we assume that the first three moments $m^{(1)}$, $c^{(2)}$ and $c^{(3)}$ are known, as well as the real-space correlation function ξ_R, we directly measure them from the simulation. We also estimate from the simulation the overall line-of-sight pairwise velocity PDF $\mathcal{P}$, which we use as a reference for model comparison. The procedures adopted for all these measurements are reported in Appendix A.

In Fig. 3, we present the redshift-space two-dimensional correlation function $\xi_S(s_\perp, s_\parallel)$ obtained via the streaming model, equation (1), with various assumptions, and compare these with the measured velocity PDF (see Appendix E for the correspondent fractional deviations). The lines represent:

(i) direct measure of the velocity PDF from the simulations, black dashed;

(ii) direct measure of the first three moments from the simulations plus GQG assumption for the velocity PDF, red solid;

Downloaded from https://academic.oup.com/mnras/article/463/4/3783/2646355 by Divisione Coordinamento Biblioteche Milano user on 09 November 2021

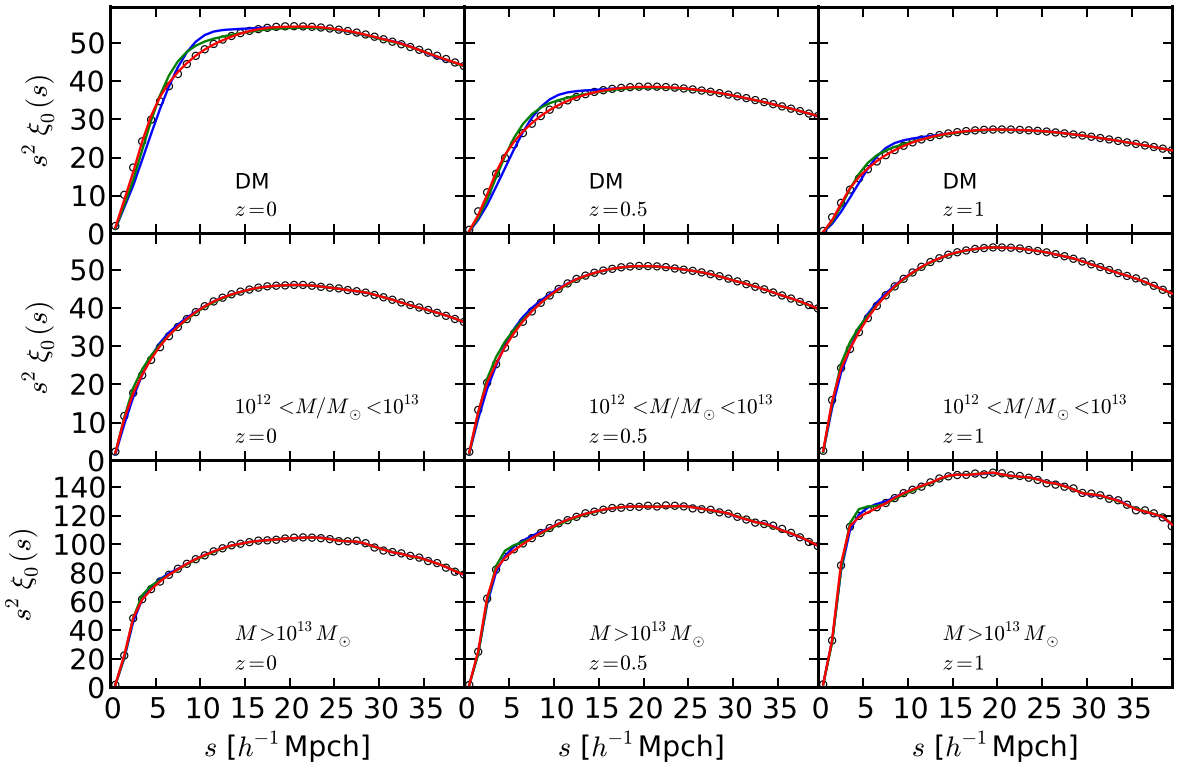

Figure 4. Legendre monopole of the redshift-space correlation function $\xi_0(s)$ as a function of the redshift-space separation s, for different tracers and redshifts as labelled in the figure. Following common practice, on the y-axis we report $s^2\xi_0(s)$, in order to help in the visualization of the large-scale behaviour. The lines correspond to the same models as in Fig. 3, with the same colour coding, except for the direct measurement of the velocity PDF, which is here represented by open circles.

(iii) direct measure of the first three moments from the simulations plus Edgeworth expansion for the velocity PDF, blue solid;

(iv) direct measure of the first two moments from the simulations plus univariate Gaussian assumption for the velocity PDF, green solid.

Since for each of the above we use the same 'true' real-space correlation function $\xi_R(r)$, any difference in the corresponding $\xi_S(s_\perp, s_\parallel)$ can be attributed to the impact of different assumptions on the shape of the velocity PDF. As discussed in Section 2.2, the GQG distribution requires additional knowledge of the functions φ. These latter, under the simplest possible ansatz, can be parametrized by $\kappa_\mu^{(t)}$ and $\kappa_\sigma^{(t)}$, Section 2.6. We fit these parameters to simulations. Since on large scales all the models perform well, here we focus on small-to-intermediate scales. As can be seen from the figure, for any tracer and redshift considered, the GQG prescription improves on the ESM, which in turn improves on the GSM. This is somewhat expected, given the different number of degrees of freedom of the different models (none the less, we note that on the smallest scales the GSM seems to perform slightly better than the ESM even though it has fewer degrees of freedom). Specifically, the smaller the mass of the tracer the larger the improvement provided by GQG with respect to ESM and GSM, which is also expected, since the velocity PDF becomes less and less Gaussian going from massive to less-massive haloes and then to DM.

In Figs 4–6, we plot the first three even Legendre multipoles of the redshift-space correlation function, namely the monopole $\xi_0(s)$, the quadrupole $\xi_2(s)$ and the hexadecapole $\xi_4(s)$. In general, Legendre multipoles are preferred with respect to the full two-dimensional correlation function when fitting models to the data because it is easier to estimate the correspondent covariance matrix. Monopole and quadrupole moments have been recently used for estimation of the cosmological parameters via the GSM (e.g. Samushia et al. 2014). The monopole, Fig. 4, is quite accurate for all the three models considered, with a small deviation of ESM and GSM from the expected amplitude on small scales in the DM case. This small-scale inaccuracy becomes more important when we consider the quadrupole, Fig. 5. Specifically, the ESM is biased for scales $\lesssim 10-15\,h^{-1}$ Mpc, depending on tracer and redshift, whilst the GSM starts failing on $\sim 10\,h^{-1}$ Mpc larger scales.[8] On the other hand, as already noted, on the smallest scales the deviation from the expected amplitude is more severe for the ESM. The GQG distribution is instead in good agreement with the direct measurements on all scales. A similar behaviour is found for the hexadecapole, Fig. 6. In this case the ESM fails on scales $\lesssim 15-30\,h^{-1}$ Mpc, depending on tracer and redshift, whilst the GSM is biased on all the scales considered. The GQG prescription recovers the correct amplitude on all scales, except for a deviation on small scales in the DM case. We attribute this deviation to the simplistic form we have assumed for the functions φ. Very likely, it would be possible to improve on this by allowing for more general functional forms (see appendix D for a more realistic description of the small-scale behaviour), none the less, since the

[8] With respect to a similar consistency test of the GSM reported in fig. 6 of Reid & White (2011), we note some discrepancy in the small-scale behaviour, especially for the quadrupole. The origin of this discrepancy is not clear, however the overall message of Reid and White's work, i.e. the GSM is few per cent precise on scales $\gtrsim 30\,h^{-1}$ Mpc for the monopole and quadruple of standard halo populations, is compatible with our results.

Downloaded from https://academic.oup.com/mnras/article/463/4/3783/2646355 by Divisione Coordinamento Biblioteche Milano user on 09 November 2021

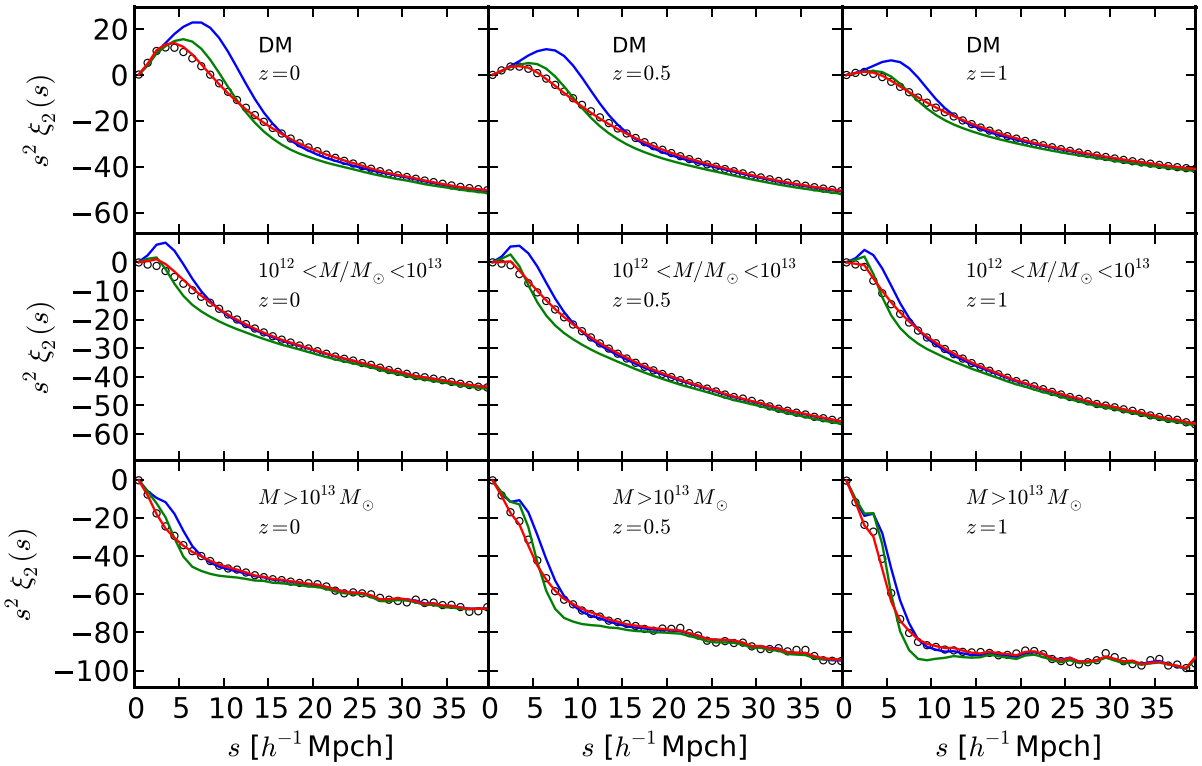

Figure 5. Same as Fig. 4 but for the quadrupole of the redshift-space correlation function $\xi_2(s)$.

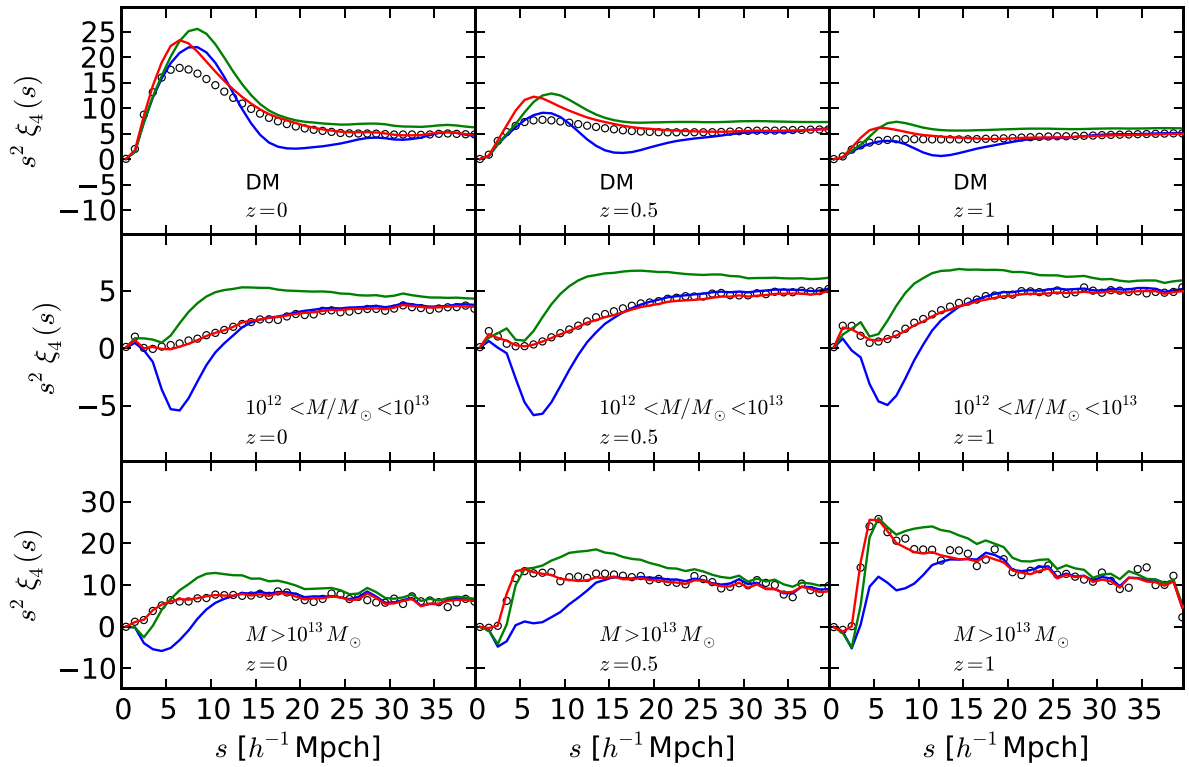

Figure 6. Same as Fig. 4 but for the hexadecapole of the redshift-space correlation function $\xi_4(s)$.

Downloaded from https://academic.oup.com/mnras/article/463/4/3783/2646355 by Divisione Coordinamento Biblioteche Milano user on 09 November 2021

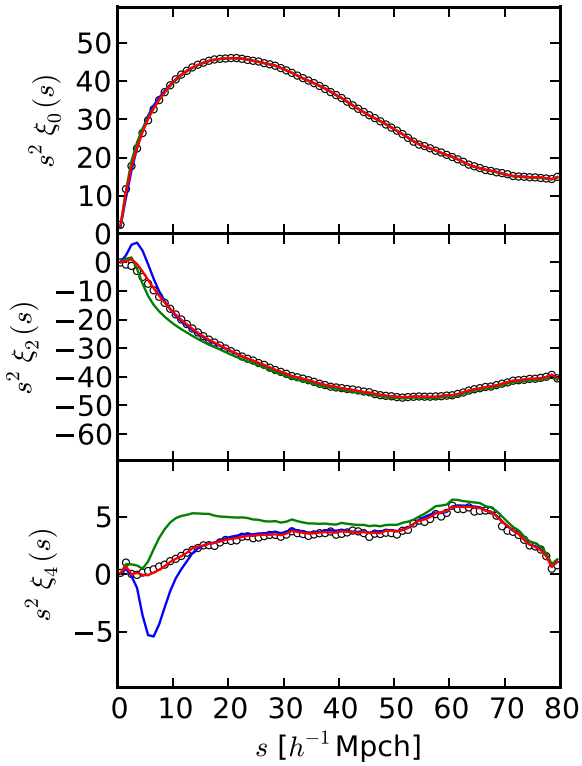

Figure 7. Legendre monopole, quadrupole and hexadecapole of the redshift-space correlation function, for the halo catalogue $10^{12} < (M/\mathrm{M}_\odot) < 10^{13}$ at $z = 0$, on a large separation range, $0 < s < 80\,h^{-1}$ Mpc. The lines correspond to the same models as in Fig. 4, with the same colour coding.

issue appears in the DM case only, in this work we prefer not to further complicate the model.

For completeness, in Fig. 7 we show the multipoles of the correlation function for the $10^{12} < (M/\mathrm{M}_\odot) < 10^{13}$ halo catalogue over a broader range of separations. As anticipated, on large scales all the three models tend to match the expected amplitude. We note however that the GSM is wrong even on moderate scales for the hexadecapole.

4 DISCUSSION AND CONCLUSIONS

It is well known that a per cent level understanding of the anisotropy of the redshift-space galaxy clustering is needed to accurately recover cosmological information from the RSD signal in order to shed light on the issue of dark energy versus modified gravity. From a statistical point of view, the source of the anisotropy is the galaxy line-of-sight pairwise velocity distribution. It is therefore important to adopt a realistic functional form for this velocity PDF when fitting models to the data. To this purpose, in Paper I we introduced the GG prescription for the velocity PDF. In this work, we have continued the development of this model by making explicit the dependence of the GG distribution on quantities predictable by theory, namely its first three moments, and extending it to the more general concept of GQG. To keep the model as simple as possible, we have proposed an ansatz with two free dimensionless parameters that describe how infall velocity and velocity dispersion vary when moving from one place to another in our Universe. Since their interpretation is clear, these parameters can be theoretically predicted or, assuming a more pragmatic approach, tuned to simulations or used as nuisance parameters. State-of-the-art PT has proven successful in predicting the large-scale behaviour of the velocity PDF and the correspondent monopole and quadrupole of the redshift-space correlation function (e.g. Reid & White 2011; Wang, Reid & White 2014), at least for massive haloes, $M \sim 10^{13}\,\mathrm{M}_\odot$. Unfortunately, by definition, any PT breaks down for small separations. Consequently, alternative approaches have been suggested in the literature, spanning from purely theoretical (e.g. Sheth 1996) to hybrid techniques in which *N*-body simulations plus an HOD are employed to deal with the issue of non-linearities (e.g. Tinker 2007; Reid et al. 2014). One of the main results from our work is to provide a framework in which perturbation and small-scale theories are smoothly joined, so that all available RSD information can be coherently extracted from redshift surveys. A fundamental requirement for a redshift-space model is that it must be precise on all scales interest, and it should inform the user of the scales on which the model can be trusted. We have compared to *N*-body simulations the well-known GSM (Reid & White 2011), the more recent ESM (Uhlemann et al. 2015) and the GQG prescription over a broad range of separations, from 0 to $80\,h^{-1}$ Mpc. Different redshifts, from $z = 0$ to 1, and different tracers, namely DM particles and two mass-selected catalogues of DM haloes, have been considered. We have concluded that, among the three, QGQ is the only model capable of providing a precise redshift-space correlation function on scales down to $\sim 5\,h^{-1}$ Mpc over the range of redshifts covered by future surveys. Keeping in mind that the range of validity of the models depends on tracer, redshift and order of the Legendre multipoles we are interested in, for finiteness, we can say that all the models converge to the expected amplitude on scales $\gtrsim 30\,h^{-1}$ Mpc, at least for multipole and quadrupole. Since these scales roughly coincide with the range of validity of state-of-the-art PTs, if we rely only on PT and if we are not interested in higher order multipoles, the most natural choice is the simplest model among the three, i.e. the GSM. As for the ESM, we have found it to be unbiased down to smaller scales and for higher order multipoles than the GSM, thus confirming the results by Uhlemann et al. (2015), but, on the other hand, it seems to behave even worse than the GSM on the smallest scales. We can therefore think of it as a natural extension of the GSM in the perspective of further PT developments. In particular, a better prediction of the third moment of the velocity PDF is required before the ESM can be applied to data on smaller scales. Formally, the same argument holds for the GQG model, none the less, since this latter is meant to include non-linear scales, it could be possible to obtain a prediction for the third moment by interpolating between (very) small and (very) large scales. More precisely, as shown in the lower-right panel of Fig. A1, the functions $c_t^{(3)}$ and $c_r^{(3)}$, which fully characterize the third moment, are peaked at $r \lesssim 10\,h^{-1}$ Mpc. By adopting a model for the small-scale limit that includes those separation, most likely using simulations in a similar way to that proposed in Reid et al. (2014), we would then be able to interpolate between these peaks and their large-scale limit, which is trivially 0.

For the above reasons, we have not tested here the performance of the of the models in recovering cosmological parameters, the growth rate f in particular. This important topic will be explored in a further work in which a prescription for the small-scale limit will be discussed. Also left for further work is an extensive test of the model on realistic mock galaxy catalogues, which very likely will give results somewhere in between those obtained for DM and haloes.

Another interesting question to be answered is whether the GQG distribution can play a role in the interpretation of the data coming from direct measurements of the velocity of galaxies (e.g. Springob

Downloaded from https://academic.oup.com/mnras/article/463/4/3783/2646355 by Divisione Coordinamento Biblioteche Milano user on 09 November 2021

et al. 2007; Tully et al. 2013), or, conversely, whether these data can be helpful in tuning the GQG parameters.

The moments of the velocity PDF on small scales are extremely sensitive to deviations from GR (e.g. Fontanot et al. 2013; Hellwing et al. 2014). Constraining these quantities is therefore of particular interest in understanding gravity. Although we have tested our model against ΛCDM simulations only, at no stage of its derivation have we assumed GR. Further investigation is clearly needed into this topic, but we do not see any obvious reason for the model not to be compatible with modified-gravity velocity PDFs and clustering.

Similarly, we do not expect baryonic physics to invalidate the GQG description, but, obviously, taking into account the impact of baryons makes the theoretical prediction of the very small scales more challenging.

Finally, we note that we have defined and analysed a very general probability distribution function, the GG distribution, which could prove useful in completely different fields. As a generalization, we have also introduced the GQG distributions, which is formally a pseudo-distribution, since for extreme values of the local skewness it can assume negative amplitude. It is none the less important to note that, at variance with what we have found for the standard Edgeworth expansion, in our measurements this unphysical situation never occurs.

ACKNOWLEDGEMENTS

DB and WJP are grateful for support from the European Research Council through the grant 614030 'Darksurvey'. WJP is also grateful for support from the UK Science and Technology Facilities Research Council through the grant ST/I001204/1. JB acknowledges support of the European Research Council through the Darklight ERC Advanced Research Grant (#291521).

REFERENCES

Bernardeau F., Colombi S., Gaztañaga E., Scoccimarro R., 2002, Phys. Rep., 367, 1
Bianchi D., Chiesa M., Guzzo L., 2015, MNRAS, 446, 75 (Paper I)
Blinnikov S., Moessner R., 1998, A&AS, 130, 193
Davis M., Peebles P. J. E., 1983, ApJ, 267, 465
Fisher K. B., 1995, ApJ, 448, 494
Fontanot F., Puchwein E., Springel V., Bianchi D., 2013, MNRAS, 436, 2672
Hamilton A. J. S., 1998, in Hamilton D., ed., Astrophysics and Space Science Library Vol. 231, The Evolving Universe. Kluwer, Dordrecht, p. 185
Hellwing W. A., Barreira A., Frenk C. S., Li B., Cole S., 2014, Phys. Rev. Lett., 112, 221102
Jackson J. C., 1972, MNRAS, 156, 1p
Juszkiewicz R., Fisher K. B., Szapudi I., 1998, ApJ, 504, L1
Kaiser N., 1987, MNRAS, 227, 1
Kwan J., Lewis G. F., Linder E. V., 2012, ApJ, 748, 78
Matsubara T., 2008, Phys. Rev. D, 78, 083519
Prada F., Klypin A. A., Cuesta A. J., Betancort-Rijo J. E., Primack J., 2012, MNRAS, 423, 3018
Reid B. A., White M., 2011, MNRAS, 417, 1913
Reid B. A., Seo H.-J., Leauthaud A., Tinker J. L., White M., 2014, MNRAS, 444, 476
Samushia L. et al., 2014, MNRAS, 439, 3504
Saunders W., Rowan-Robinson M., Lawrence A., 1992, MNRAS, 258, 134
Scoccimarro R., 2004, Phys. Rev. D, 70, 083007
Seljak U., McDonald P., 2011, J. Cosmol. Astropart. Phys., 11, 39
Sheth R. K., 1996, MNRAS, 279, 1310
Springob C. M., Masters K. L., Haynes M. P., Giovanelli R., Marinoni C., 2007, ApJS, 172, 599
Taruya A., Nishimichi T., Saito S., 2010, Phys. Rev. D, 82, 063522
Tinker J. L., 2007, MNRAS, 374, 477
Tully R. B. et al., 2013, AJ, 146, 86
Uhlemann C., Kopp M., Haugg T., 2015, Phys. Rev. D, 92, 063004
Wang L., Reid B., White M., 2014, MNRAS, 437, 588
Zurek W. H., Quinn P. J., Salmon J. K., Warren M. S., 1994, ApJ, 431, 559

APPENDIX A: MEASUREMENTS OF VELOCITY PDF, MOMENTS AND CORRELATION FUNCTION FROM SIMULATIONS

Ignoring wide-angle effects, the line-of-sight pairwise velocity distribution $\mathcal{P}(v_\parallel|r_\perp, r_\parallel)$ is obtained by projecting along the line of sight the two-dimensional pairwise velocity distribution $\mathcal{P}_r(v_r, v_t|r)$. This latter is the joint distribution of the parallel (v_r) and perpendicular (v_t) components of the pairwise velocity with respect to the pair separation $\boldsymbol{r}$. Due to isotropy it depends only on the length r of the separation vector. Although measurements of $\mathcal{P}$ and $\mathcal{P}_r$ are formally equivalent, we prefer to adopt the second approach since it allows us to take advantage of all possible symmetries, thus minimizing statistical noise and cosmic variance (in essence, we do not need to choose a line of sight).

Similarly, the moments of the pairwise-velocity PDF can be decomposed as follows (e.g. Uhlemann et al. 2015),

$$m^{(1)}(r, \mu_\theta) = m_r^{(1)}(r)\, \mu_\theta \tag{A1}$$

$$c^{(2)}(r, \mu_\theta) = c_r^{(2)}(r)\, {\mu_\theta}^2 + c_t^{(2)}(r)\left(1 - {\mu_\theta}^2\right) \tag{A2}$$

$$c^{(3)}(r, \mu_\theta) = \left[c_r^{(3)}(r)\, {\mu_\theta}^2 + c_t^{(3)}(r)\left(1 - {\mu_\theta}^2\right)\right] \mu_\theta, \tag{A3}$$

where $r = \sqrt{{r_\perp}^2 + {r_\parallel}^2}$, $\mu_\theta = r_\parallel/r$ and we have used the fact that, because of isotropy, the only non-vanishing correlators between the radial and tangential component of the pairwise velocity are those involving even powers (i.e. the modulus) of the tangential component. Here, for self-consistency and to minimize the statistical noise, it is convenient to follow a scheme that is somehow opposite to what we do for the PDF: from $\mathcal{P}$ we measure the left-hand term of these equations, but our model requires as an input the radial-dependent functions on the right-hand side, which is what is usually predicted in PT. We then need to invert this set of equations. From equation (A1) we get

$$m_r^{(1)}(r) = \frac{1}{\Delta\mu_\theta} \int_{\Delta\mu_\theta} \mathrm{d}\mu_\theta\, \frac{m^{(1)}(r, \mu_\theta)}{\mu_\theta}, \tag{A4}$$

where the integral can in principle be performed over any arbitrary interval $\Delta\mu_\theta = \mu_\theta^{\max} - \mu_\theta^{\min}$, with $0 < \mu_\theta^{\min} < \mu_\theta^{\max} < 1$. Similarly, equation (A2) yields

$$c_r^{(2)}(r) = \frac{1}{\Delta\mu_\theta} \int_{\Delta\mu_\theta} \mathrm{d}\mu_\theta \left[\frac{2}{3\mu_\theta^2 - 1}\, c^{(2)}(r, \mu_\theta) - \frac{2(1 - {\mu_\theta}^2)}{3{\mu_\theta}^2 - 1}\, \bar{c}^{(2)}(r)\right] \tag{A5}$$

$$c_t^{(2)}(r) = \frac{1}{\Delta\mu_\theta} \int_{\Delta\mu_\theta} \mathrm{d}\mu_\theta \left[\frac{1}{1 - 3\mu_\theta^2}\, c^{(2)}(r, \mu_\theta) - \frac{3\mu_\theta^2}{1 - 3\mu_\theta^2}\, \bar{c}^{(2)}(r)\right], \tag{A6}$$

Downloaded from https://academic.oup.com/mnras/article/463/4/3783/2646355 by Divisione Coordinamento Biblioteche Milano user on 09 November 2021

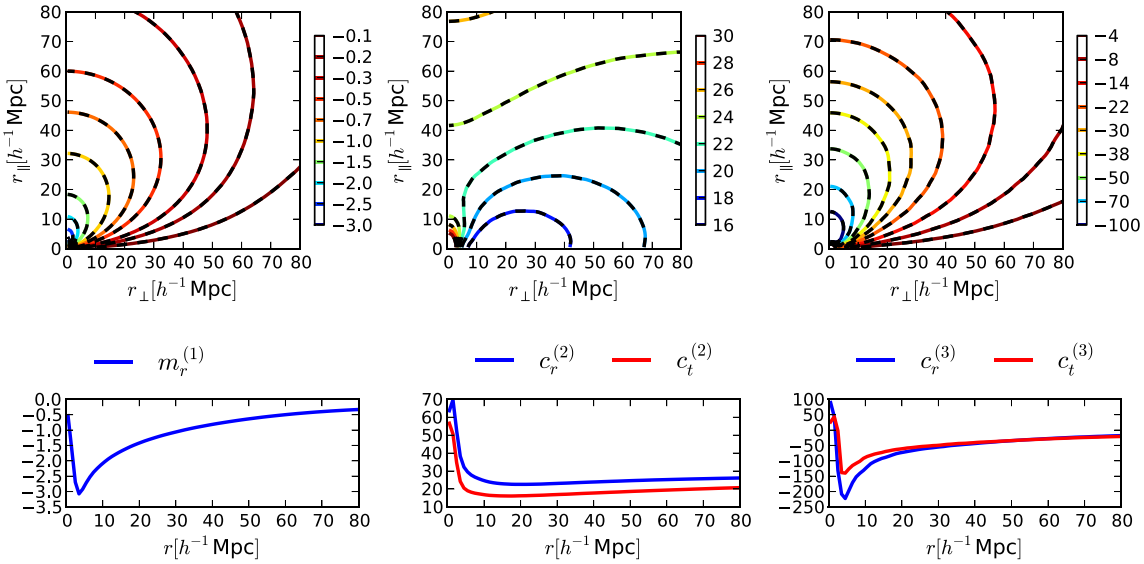

Figure A1. Moments of the line-of-sight pairwise velocity distribution for the DM catalogue at $z = 0$ (the velocity is measured in units of length via the standard $\mathcal{H}^{-1}$ rescaling). Upper panels, from left to right: first moment $m^{(1)}$, second central moment $c^{(2)}$ and third central moment $c^{(3)}$, presented using iso-amplitude contours as a function of the real-space separation parallel and perpendicular to the line of sight, $r_\parallel$ and $r_\perp$, respectively. Different lines represents: direct measurements of the moments from simulations, solid coloured, reconstruction of the moments via equations (A1), (A2) and (A3). Lower panels: measurements of the parallel and perpendicular (with respect to the real-space separation vector $\boldsymbol{r}$) component of the moments as a function of r, as labelled in the figure. These functions are used as input for computing the dashed lines in the correspondent upper panel.

where we have defined

$$\bar{c}^{(2)}(r) = \int_0^1 \mathrm{d}\mu_\theta \, c^{(2)}(r, \mu_\theta). \tag{A7}$$

Finally, from equation (A3) we obtain

$$c_r^{(3)}(r) = \frac{1}{\Delta\mu_\theta} \int_{\Delta\mu_\theta} \mathrm{d}\mu_\theta \left[\frac{1}{\mu_\theta \left(2\mu_\theta^2 - 1\right)} c^{(3)}(r, \mu_\theta) - \frac{4\left(1-\mu_\theta^2\right)}{2\mu_\theta^2 - 1} \bar{c}^{(3)}(r) \right] \tag{A8}$$

$$c_t^{(3)}(r) = \frac{1}{\Delta\mu_\theta} \int_{\Delta\mu_\theta} \mathrm{d}\mu_\theta \left[\frac{1}{\mu_\theta \left(1 - 2\mu_\theta^2\right)} c^{(3)}(r, \mu_\theta) - \frac{4\mu_\theta^2}{1 - 2\mu_\theta^2} \bar{c}^{(3)}(r) \right], \tag{A9}$$

where

$$\bar{c}^{(3)}(r) = \int_0^1 \mathrm{d}\mu_\theta \, c^{(3)}(r, \mu_\theta). \tag{A10}$$

Clearly, the larger $\Delta\mu_\theta$ the more information we include in our analysis, none the less two potential issues have to be considered.

(i) For $\mu_\theta = 1$ the integrals might diverge. This problem is naturally solved by the fact that the moments are measured in bins of μ_θ, which means that the largest available $\mu_\theta^{\max}$ is always smaller than 1.

(ii) Since the odd moments vanish for $\mu_\theta \to 0$ [equations (A1) and (A3)], including small values of μ_θ in our analysis only add instability. For these moments we then safely adopt $\mu_\theta^{\min} = 0.5$.

In the left upper panel of Fig. A1, we compare the direct measurement from $\mathcal{P}$ of the first moment $m^{(1)}$ (solid lines) with that obtained by estimating $m_r^{(1)}$ via equation (A4) and then multiplying by μ_θ (dashed lines). In other words, we test the validity of our approach by comparing left- with right-hand side of equation (A1). We do the same for the less trivial measurements of $c^{(2)}$ and $c^{(3)}$, central and right upper panel, respectively. Only contours from the DM catalogue at $z = 0$ are shown but all tracers and redshift considered yield similar results. We also report in the lower panels the underling decomposition of the moments. Given the good match seen in the figures, we can conclude that our procedure to decompose the moments works properly and will not introduce any kind of bias in our final results.

For the estimation of correlation function we adopt the natural estimator $\xi = \frac{\mathrm{DD}}{\mathrm{RR}} - 1$, where DD and RR represent the number of data and random pairs at a given separation, respectively. This is the most natural choice when dealing with periodical boxes, in which there are no border effects and RR can be computed analytically.

For all the measurements in this work, we adopt linear bins of $1\,h^{-1}$ Mpc size [note that, since we use the standard $\mathcal{H}^{-1}$ rescaling (see e.g. Scoccimarro 2004), the velocities are measured in unit of length].

APPENDIX B: DETAILS ON THE MOMENT GENERATING FUNCTION

For the sake of completeness, in Table B1 we report the MGF of the GG distribution for a few specific combinations of the parameter set $\{M_\mu, M_\sigma, C_{\mu\mu}, C_{\sigma\sigma}, C_{\mu\sigma}\}$. Specifically, from top to bottom we show:

(i) The MGF of the full distribution.

(ii) The zero-skewness limit, $C_{\mu\sigma} = 0$. This is the limit of the GG distribution for $\mu_\theta \to 0$ where the skewness disappears by symmetry.

(iii) The maximum-skewness limit, $M_\sigma^2 = C_{\mu\mu} = C_{\sigma\sigma}$. Since, as shown in Section 2.4, for this combination of the parameters the conversion of covariance in skewness is maximized, we assumed this limit for $\mu_\theta \to 1$. Note however that, in order to match simulations, we have to correct for the skewness by using GQG, Section 2.5.

Downloaded from https://academic.oup.com/mnras/article/463/4/3783/2646355 by Divisione Coordinamento Biblioteche Milano user on 09 November 2021

Table B1. Moment generating function of the GG distribution (central column) for different assumptions on the parameters M_μ, M_σ, $C_{\mu\mu}$, $C_{\sigma\sigma}$ and $C_{\mu\sigma}$ (left-hand column). In the right-hand column is reported the number of free parameters.

Assumptions	Moment generating function	n.f.p.
–	$\frac{1}{\sqrt{1-t^2C_{\sigma\sigma}}}\exp\left\{tM_\mu+\frac{1}{2}t^2{M_\sigma}^2+\frac{1/2}{1-t^2C_{\sigma\sigma}}\left[t^2C_{\mu\mu}+2t^3C_{\mu\sigma}M_\sigma+t^4\left({M_\sigma}^2C_{\sigma\sigma}-\det C\right)\right]\right\}$	5
$C_{\mu\sigma}=0$	$\frac{1}{\sqrt{1-t^2C_{\sigma\sigma}}}\exp\left\{tM_\mu+\frac{1}{2}t^2{M_\sigma}^2+\frac{1/2}{1-t^2C_{\sigma\sigma}}\left[t^2C_{\mu\mu}+t^4C_{\sigma\sigma}\left({M_\sigma}^2-C_{\mu\mu}\right)\right]\right\}$	4
${M_\sigma}^2=C_{\mu\mu}=C_{\sigma\sigma}$	$\frac{1}{\sqrt{1-t^2{M_\sigma}^2}}\exp\left\{tM_\mu+\frac{1}{1-t^2{M_\sigma}^2}\left[t^2{M_\sigma}^2+t^3C_{\mu\sigma}M_\sigma+t^4\left(C_{\mu\sigma}-\frac{1}{2}{M_\sigma}^4\right)\right]\right\}$	3
$C_{\sigma\sigma}=C_{\mu\sigma}=0$	$\exp\left[tM_\mu+\frac{1}{2}t^2\left({M_\sigma}^2+C_{\mu\mu}\right)\right]$	3
$C_{\mu\mu}=C_{\mu\sigma}=0$	$\frac{1}{\sqrt{1-t^2C_{\sigma\sigma}}}\exp\left(tM_\mu+\frac{\frac{1}{2}t^2{M_\sigma}^2}{1-t^2C_{\sigma\sigma}}\right)$	3
$C_{\mu\mu}=C_{\mu\sigma}=0,\quad {M_\sigma}^2=2C_{\sigma\sigma}$	$\frac{1}{\sqrt{1-t^2C_{\sigma\sigma}}}\exp\left(tM_\mu+\frac{t^2C_{\sigma\sigma}}{1-t^2C_{\sigma\sigma}}\right)$	2
$M_\sigma=C_{\mu\mu}=C_{\mu\sigma}=0$	$\frac{1}{\sqrt{1-t^2C_{\sigma\sigma}}}\exp\left(tM_\mu\right)$	2

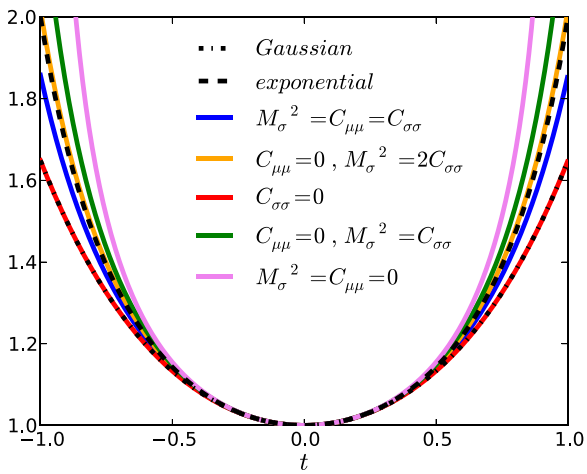

Figure B1. Moment generating functions of the GG distribution for different combinations of the parameters M_σ, $C_{\mu\mu}$ and $C_{\sigma\sigma}$ as labelled in the figure, solid coloured. Only the zero-skewness case is considered, i.e. $C_{\mu\sigma}=0$. For comparison, we also show the moment generating function of Gaussian and exponential distributions, black dot–dashed and black dashed, respectively. All the curves are standardized, i.e. zero mean and unit variance.

(iv) The Gaussian limit, $C_{\sigma\sigma=0}$. This limit has been discussed in Section 2.1. When the further condition $C_{\mu\mu=0}$ is added, we obtain a very natural large scale limit.

(v) The small-scale limit, $C_{\mu\mu}=C_{\mu\sigma}=0$. As discussed in Section 2.1 and, more extensively, in Appendix D, this is the behaviour we expect at very small separations, where the infall velocity disappears.

(vi) The quasi-exponential limit, $C_{\mu\mu}=C_{\mu\sigma}=0$ and ${M_\sigma}^2=2C_{\sigma\sigma}$. The MGF of an exponential is $\exp(\mu t)/(1-\frac{1}{2}\sigma^2t^2)$, where μ is the mean and σ^2 the variance, which clearly differs from what is reported in the table. None the less we, show in Fig. B1 that for this combination of the parameters the MGFs of the two distributions behave in a very similar way.

(vii) The combination $M_\sigma=C_{\mu\mu}=C_{\mu\sigma}=0$, which, formally, is another sub case of the small-scale limit. Although we have not explicitly used such combinations it in this work, it is by itself interesting to see how simple becomes the MGF under this condition. As far as we know, this do not correspond to the MGF of any common distribution but it helps us in showing how wide is the parameter space spanned by the GG distribution, see Fig. B1.

In Fig. B1, we show the MGF of the GG distribution for the combination of parameters discussed above (coloured solid). For comparison, we also report the MGF of Gaussian and exponential distribution (black dot–dashed and black dashed, respectively). All the functions have zero mean, unitary variance and zero skewness. It is clear from the figure that the GG distribution efficiently covers the space between Gaussian and exponential distribution and beyond.

APPENDIX C: BIVARIATE DISTRIBUTION OF μ AND $\sqrt{\sigma}$ AS AN ALTERNATIVE WAY TO ALLOW FOR MORE SKEWNESS

Most of the calculations presented in this paper can be easily extended to the case in which the jointly distributed variables are μ and $\sigma^{\frac{1}{2n}}$, with $n\in N$, rather than μ and σ. Here we discuss the specific scenario in which $n=1$, i.e. μ and $\psi\equiv\sqrt{\sigma}$ are jointly distributed according to a bivariate Gaussian. Since, as shown in the following, the resulting upper limit for the skewness of the velocity PDF is higher than that of a standard GG distribution, this approach potentially represents a viable alternative to GQG in solving the skewness issue, Section 2.4.

The integration over μ still gives equation (8) but, obviously, with different expressions for $\mathcal{A}$ and $\mathcal{K}_i$,

$$\mathcal{A}^2=C_{\psi\psi}\psi^4+C_{\mu\mu}C_{\psi\psi}-{C_{\mu\psi}}^2 \tag{C1}$$

$$\mathcal{K}_2=C_{\psi\psi} \tag{C2}$$

$$\mathcal{K}_1=-2C_{\mu\psi}\left(\psi-M_\psi\right) \tag{C3}$$

$$\mathcal{K}_0=\left(\psi^4+C_{\mu\mu}\right)\left(\psi-M_\psi\right)^2. \tag{C4}$$

As for the first three moments, we obtain

$$m^{(1)}=M_\mu \tag{C5}$$

$$c^{(2)}={M_\psi}^4+C_{\mu\mu}+6{M_\psi}^2C_{\psi\psi}+3{C_{\psi\psi}}^2 \tag{C6}$$

$$c^{(3)}=12\left({M_\psi}^3+3M_\psi C_{\psi\psi}\right)C_{\mu\psi}. \tag{C7}$$

We can express equation (C7) in terms of the correlation coefficient $\rho=C_{\mu\psi}/\sqrt{C_{\mu\mu}C_{\psi\psi}}$,

$$c^{(3)}=12\rho\sqrt{\left({M_\psi}^3+3M_\psi C_{\psi\psi}\right)^2C_{\mu\mu}C_{\psi\psi}} \tag{C8}$$

Downloaded from https://academic.oup.com/mnras/article/463/4/3783/2646355 by Divisione Coordinamento Biblioteche Milano user on 09 November 2021

In analogy to what we have done in Section 2.3, we define

$$\varphi_{M\psi} \equiv \frac{{M_\psi}^2}{\sqrt{c^{(2)}}} \quad \varphi_{C\psi\psi} \equiv \sqrt{\frac{3}{c^{(2)}}} C_{\psi\psi} \quad \varphi_{C\mu\mu} \equiv \frac{C_{\mu\mu}}{c^{(2)}}, \tag{C9}$$

for which holds the relation

$$\varphi_{C\mu\mu} + \varphi_{M\psi}^2 + 2\sqrt{3}\varphi_{M\psi}\varphi_{C\psi\psi} + \varphi_{C\psi\psi}^2 = 1. \tag{C10}$$

We then rewrite equation (C8) as

$$c^{(3)} = 4(\sqrt{3}c^{(2)})^{3/2}\rho(\varphi_{M\psi} + \sqrt{3}\varphi_{C\psi\psi})\sqrt{\varphi_{M\psi}\varphi_{C\psi\psi}\varphi_{C\mu\mu}}. \tag{C11}$$

Since by construction $|\rho| < 1$, form equations (C10) and (C11) we can assess the upper limit for the skewness $\gamma = \frac{c^{(3)}}{c^{(2)^{3/2}}}$. Specifically, we obtain $|\gamma| \lesssim 1.85$, which is ∼60 per cent larger than what we get for a standard GG distribution, Section 2.4.

APPENDIX D: SMALL-SCALE LIMIT

For very small separations, $r \to 0$, the velocity statistics is dominated by pairs inside virialized region, we therefore expect the local infall velocity to disappear, which implies $M_\mu = C_{\mu\mu} = 0$. Note that the latter equality requires $C_{\mu\sigma} = 0$ as well. By substituting in equation (8) we find

$$\mathcal{P} = \int \mathrm{d}\sigma \, \frac{\mathcal{W}}{\sqrt{2\pi\sigma^2}} \exp\left(-\frac{{v_\parallel}^2}{2\sigma^2}\right), \tag{D1}$$

where

$$\mathcal{W} \equiv \frac{1}{\sqrt{2\pi C_{\sigma\sigma}}} \exp\left[-\frac{(\sigma - M_\sigma)^2}{2C_{\sigma\sigma}}\right]. \tag{D2}$$

Following the same reasoning behind equations (6) and (7), we define

$$\mathcal{W}^\pm(\sigma) \equiv \mathcal{W}(-\sigma) + \mathcal{W}(\sigma) = \sqrt{\frac{2}{\pi C_{\sigma\sigma}}} \exp\left(-\frac{\sigma^2 + {M_\sigma}^2}{2C_{\sigma\sigma}}\right) \cosh\left(\frac{M_\sigma \sigma}{C_{\sigma\sigma}}\right), \tag{D3}$$

so that we can rewrite equation (D1) as an integral over a non-negative range,

$$\mathcal{P} = \int_0^{+\infty} \mathrm{d}\sigma \, \frac{\mathcal{W}^\pm}{\sqrt{2\pi\sigma^2}} \exp\left(-\frac{{v_\parallel}^2}{2\sigma^2}\right). \tag{D4}$$

In this small-scale scenario, at any given position in the universe, the pairs contributing to the corresponding local velocity PDF all belong to the same halo. We can therefore infer the variance σ^2, which is the only remaining local parameter, from consideration on the physical properties of a single isolated halo. A useful discussion about this topic can be found in Sheth (1996), in which, under the assumption that haloes are virialized and isothermal systems, an expression for $\sigma = \sigma(M)$ is derived, where M is the mass of the halo. If we compare equation (D4) with the corresponding expression for the small-scale velocity PDF derived by Sheth, his equation 5, we realize that $\mathcal{W}^\pm$ is essentially the probability $\mathcal{T}(M)$ that a pair with separation r belongs to an halo of mass M. More specifically, for any fixed (small) separation r, Sheth (1996) comes to the following integral,

$$\mathcal{P} = \int_0^{+\infty} \mathrm{d}M \, \frac{\theta(M - M_{\min})\, \mathcal{T}(M)}{\sqrt{2\pi\sigma(M)^2}} \exp\left(-\frac{{v_\parallel}^2}{2\sigma(M)^2}\right), \tag{D5}$$

where θ is a step function and $M_{\min}$ is the minimum halo mass compatible with the separation r. From equations (D4) and (D5), it follows that $\mathcal{W}^\pm$ can be seen as a two-parameter ansatz for the function $|\mathrm{d}M/\mathrm{d}\sigma| \, \theta[M(\sigma) - M_{\min}] \, \mathcal{T}[M(\sigma)]$. As shown by Sheth (1996), under reasonable physical assumptions, this latter can be computed once a mass function is provided.

A straightforward procedure to include this theoretical prediction for the small-scale limit in our model can be obtained as follows. From Table 2, it is easy to see that in the small-scale limit $\mathcal{P}$ can be expressed as a function of its first two even central moments $c^{(2)}$ and $c^{(4)}$,

$${M_\sigma}^2 = \sqrt{\frac{3}{2}c^{(2)^2} - \frac{1}{6}c^{(4)}} \tag{D6}$$

$$C_{\sigma\sigma} = c^{(2)} - {M_\sigma}^2. \tag{D7}$$

We then need a theoretical prediction of these two moments. Form equation (D5), it follows

$$c^{(n)} = \int_{M_{\min}}^{+\infty} \mathrm{d}M \, 3^{\frac{n-2}{2}} \sigma(M)^n \, \mathcal{T}(M) \tag{D8}$$

for $n = 2, 4$, which completes the modelling.

It should be noted that if we want to adapt the model introduced in Section 2.2 to the small-scale limit just discussed, a decreasing (or even flat, as proposed in Section 2.6) profile for the function $\varphi_{C\mu\mu}$ is no longer acceptable. More explicitly, a decreasing profile implies that if $\lim_{r\to 0} C_{\mu\mu} = 0$, then $C_{\mu\mu} = 0$ at any separation, which means $C_{\mu\sigma} = 0$ at any separation as well. A more general profile for the functions φ is then required. The simplest possible improvement is to define a scale r_3 below which $\varphi_{C\mu\mu}$, more precisely its parallel and perpendicular components, is damped. Since, based on the discussion in Section 2.4, we expect this scale to roughly correspond the skewness maximum, from the right-hand panels of Fig. A1 we can argue that $r_3 \sim 5\,h^{-1}$ Mpc.

APPENDIX E: PRECISION OF THE MODEL

For completeness, in Fig. E1 we explicitly show the ratio between the $\xi_S(s_\perp, s_\parallel)$ corresponding to the three models discussed in this work, GQG, GSM and ESM (red, green and blue solid lines in Fig. 3), with respect to the reference one obtained by measuring the velocity PDF directly from the simulations (black dashed lines in Fig. 3). Only $z = 0$ is considered, but different redshifts yield similar results. As expected, GQG outperforms GSM and ESM, being per cent accurate almost everywhere. The residual small-scale discrepancies can in principle be removed by improving the modelling of the φ functions. We leave this topic to further work.

Downloaded from https://academic.oup.com/mnras/article/463/4/3783/2646355 by Divisione Coordinamento Biblioteche Milano user on 09 November 2021

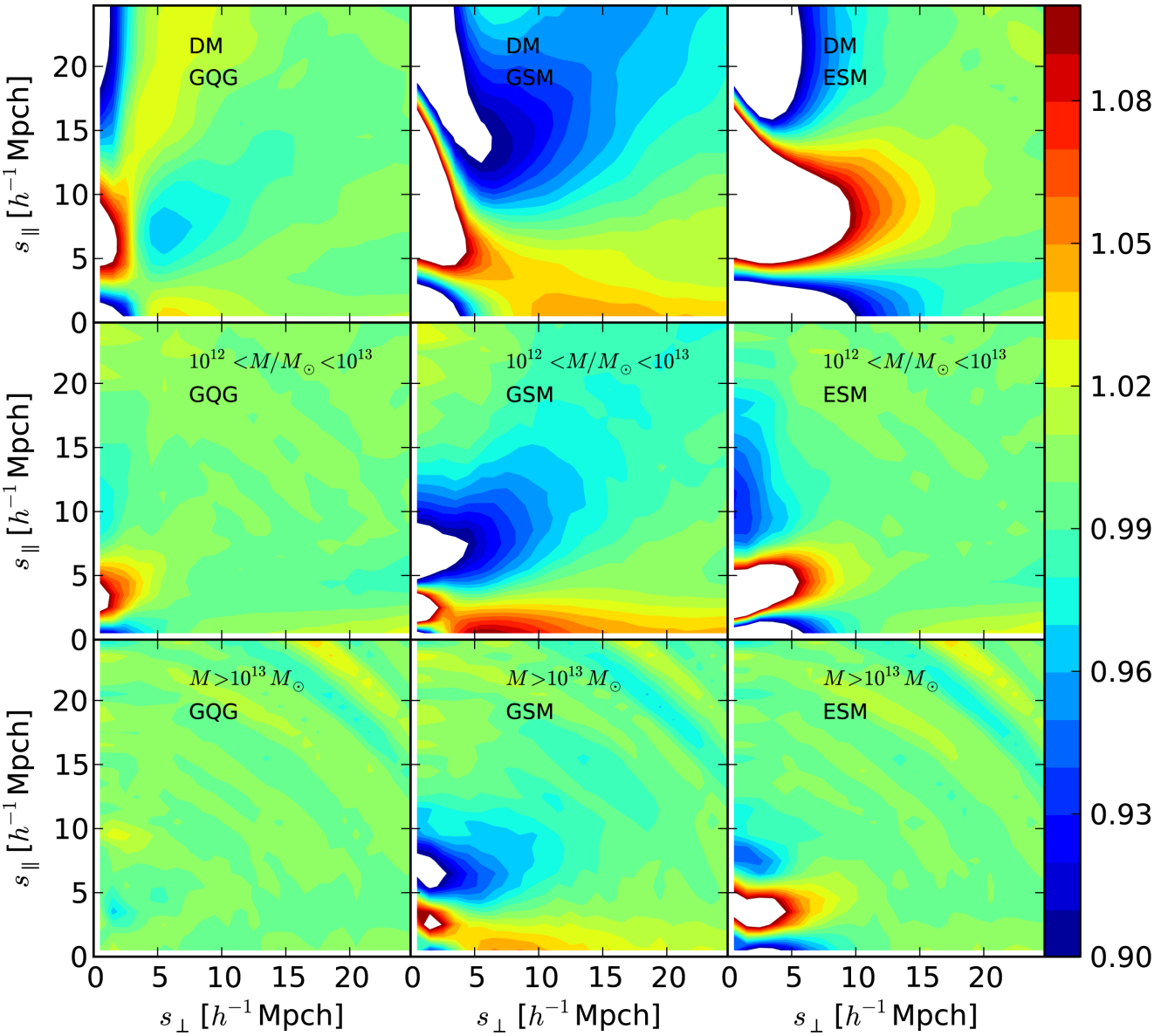

Figure E1. Colour map of the ratio, at $z = 0$, between the two-dimensional correlation function obtained via GQG (left-hand panels), GSM (central panels) and ESM (right-hand panels) with respect to that obtained by measuring the velocity PDF directly from the simulations, for different tracers as labelled in the figure.

This paper has been typeset from a TEX/LATEX file prepared by the author.

Downloaded from https://academic.oup.com/mnras/article/463/4/3783/2646355 by Divisione Coordinamento Biblioteche Milano user on 09 November 2021